# nature photonics

**Article** 

https://doi.org/10.1038/s41566-022-01086-9

# A full degree-of-freedom spatiotemporal light modulator

Received: 16 May 2022

Accepted: 11 September 2022

Published online: 28 November 2022



Christopher L. Panuski ®¹⊠, Ian Christen¹, Momchil Minkov², Cole J. Brabec¹, Sivan Trajtenberg-Mills¹, Alexander D. Griffiths³, Jonathan J. D. McKendry ®³, Gerald L. Leake⁴, Daniel J. Coleman⁴, Cung Tran⁴, Jeffrey St Louis⁴, John Mucci⁴, Cameron Horvath⁵, Jocelyn N. Westwood-Bachman ®⁵, Stefan F. Preble⁶, Martin D. Dawson ®³, Michael J. Strain ®³, Michael L. Fanto⁵ & Dirk R. Englund ®¹⊠

Harnessing the full complexity of optical fields requires the complete control of all degrees of freedom within a region of space and time—an open goal for present-day spatial light modulators, active metasurfaces and optical phased arrays. Here, we resolve this challenge with a programmable photonic crystal cavity array enabled by four key advances: (1) near-unity vertical coupling to high-finesse microcavities through inverse design; (2) scalable fabrication by optimized 300 mm full-wafer processing; (3) picometre-precision resonance alignment using automated, closed-loop 'holographic trimming'; and (4) out-of-plane cavity control via a high-speed µLED array. Combining each, we demonstrate the near-complete spatiotemporal control of a 64 resonator, two-dimensional spatial light modulator with nanosecond- and femtojoule-order switching. Simultaneously operating wavelength-scale modes near the spacebandwidth and time—bandwidth limits, this work opens a new regime of programmability at the fundamental limits of multimode optical control.

Programmable optical transformations are of fundamental importance across science and engineering, from adaptive optics in astronomy and neuroscience  $^{2,3}$  to dynamic matrix operations in machine learning  $^{4-6}$  and quantum computing  $^{7,8}$ . Despite this importance, the high-resolution manipulation of multimode optical fields—the central objective of spatial light modulators (SLMs)—remains an open challenge  $^9$ . Specifically, the limited modulation bandwidth and/or pixel density of liquid-crystal- or micromirror-based SLMs  $^{10,11}$ , optical phased arrays  $^{12,13}$  and active metasurfaces  $^{14-17}$  prevent the complete control of optical fields tuned by them  $^{18}$ .

Figure 1a illustrates the limitations of current SLMs, which typically comprise a two-dimensional (2D),  $\Lambda$ -pitch array of tunable pixels (subscript p) emitting at wavelength  $\lambda$  into solid angle  $\Omega_p$  with a system (subscript s) modulation bandwidth  $\omega_s$ . Given these parameters, each

'spatiotemporal' degree of freedom (DoF) simultaneously satisfying the minimum-uncertainty space–bandwidth and time–bandwidth relations  $(\delta A/\lambda^2 \cdot \delta \Omega = 1$  and  $\delta t \, \delta \omega = 1$ , respectively) can be illustrated as a real-space voxel with area  $\lambda^2/\Omega_p$  and time duration  $1/\omega_p$  for pixel bandwidth  $\omega_p$ . The optical-delay-limited pixel bandwidth  $\omega_p \approx (\Delta \varepsilon_p/\varepsilon)ck$  can be perturbatively approximated as a function of the achievable permittivity swing  $\Delta \varepsilon_p$  (for speed of light c) or similarly derived from linear scattering theorems<sup>19</sup>.

Integrating over the switching interval  $T = 1/\omega_s$  and aperture area A then gives the total DoF count<sup>18</sup>

$$F = \int_{A,\Omega_{\mathbf{p}}} \frac{\mathrm{d}A}{\lambda^2} \mathrm{d}\Omega \int_{T,\omega_{\mathbf{p}}} \mathrm{d}t \mathrm{d}\omega. \tag{1}$$

<sup>1</sup>Research Laboratory of Electronics, Massachusetts Institute of Technology, Cambridge, MA, USA. <sup>2</sup>Flexcompute, Belmont, MA, USA. <sup>3</sup>Institute of Photonics, Department of Physics, University of Strathclyde, Technology and Innovation Centre, Glasgow, UK. <sup>4</sup>State University of New York Polytechnic Institute, Albany, NY, USA. <sup>5</sup>Applied Nanotools, Edmonton, Alberta, Canada. <sup>6</sup>Electrical and Microelectronic Engineering, Rochester Institute of Technology, Rochester, NY, USA. <sup>7</sup>Air Force Research Laboratory, Information Directorate, Rome, NY, USA. —e-mail: cpanuski@mit.edu; englund@mit.edu

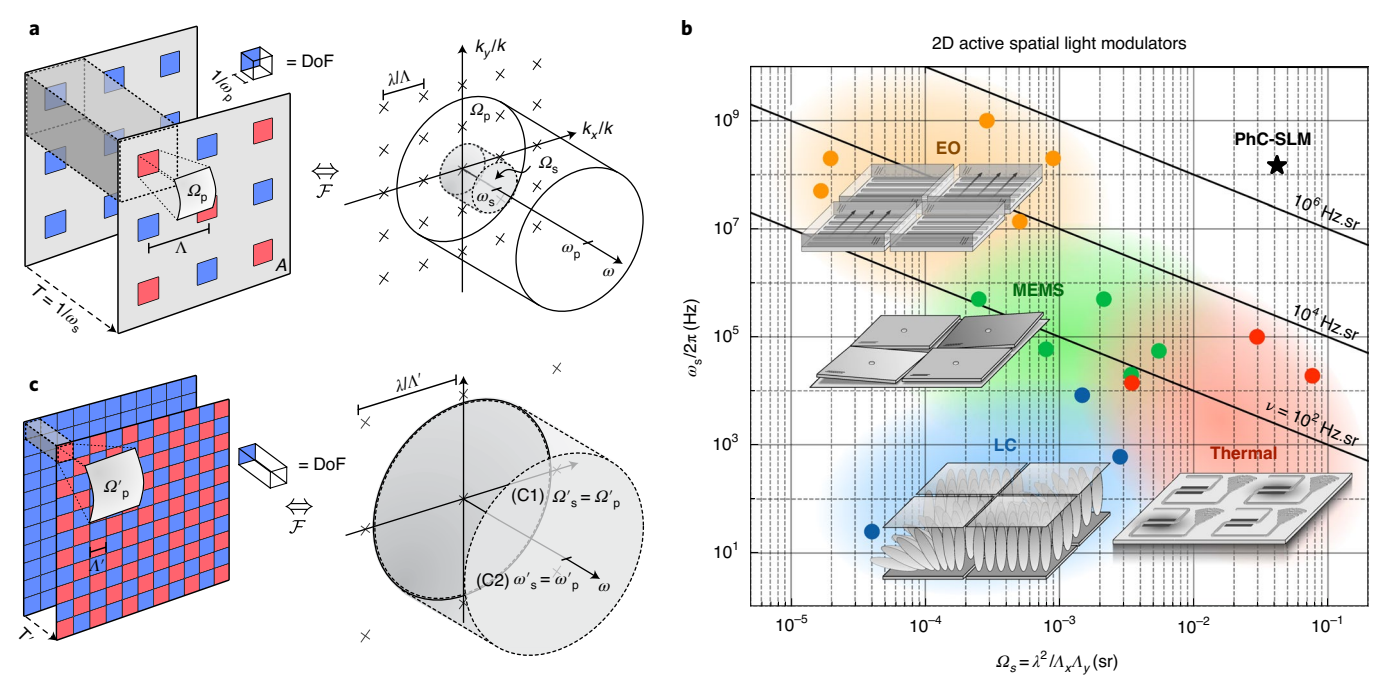


Fig. 1 | Full DoF spatiotemporal optical programming. a, Present-day SLMs feature a 2D array of Λ-pitch pixels within aperture area A. Each pixel radiates at wavenumber  $k = 2\pi/\lambda$  into solid angle  $\Omega_p$  and can be switched (blue  $\leftrightarrow$  red colour change indicates a  $\pi$ -phase change of the emitted field) over the timescale  $T = 1/\omega_s$  (given a modulation bandwidth  $\omega_s$ ) with a large but slow fractional permittivity perturbation  $\Delta \epsilon_p/\epsilon$  (liquid crystal rotation, for example). The shaded volume indicates the smallest controllable near-field spatiotemporal mode. In the far field (right), the corresponding shaded spatiotemporal bandwidth  $\nu = \Omega_s \omega_s = (\lambda/\Lambda)^2 \omega_s$  counts the controllable DoF per unit area and time in a single diffraction order. b, Trade-offs between  $\omega_s$  and  $\Omega_s$  in liquid crystal (LC)-, thermal-,

micro-electro-mechanical system (MEMS)- and electro-optic (EO)-driven SLMs (Extended Data Table 1) limit  $\nu \ll \Omega_p \omega_p$ , the accessible pixel spatiotemporal bandwidth given the delay-limited bandwidth  $\omega_p \approx ck\Delta \epsilon_p/\epsilon$ . Spatiotemporal control is thus limited and scattering into undesired diffraction orders (grey-coloured '×' symbols) reduces the diffraction efficiency.  $\mathbf{c}$ , Alternatively, a fully filled array of wavelength-scale resonant apertures emitting into the solid angle  $\Omega_p'$  can enhance the effect of fast (modulation frequency  $\omega_s'$ ), low-energy perturbations  $\Delta \epsilon_p' \ll \epsilon$  to simultaneously achieve space–bandwidth and time–bandwidth limits ((C1) and (C2), respectively), yielding near-complete spatiotemporal control with  $\nu' \approx \Omega_n' \omega_p''$ .

By comparison, the same switching period contains  $N=A/\Lambda^2 \le F$  controllable modes, each confined to pixel area  $\Lambda^2$  and time window T (Fig. 1a, shaded box). Complete spatiotemporal control with N=F is only achieved under the following criteria: (C1) emitters fully 'fill' the near-field aperture such that  $\Omega_p$  matches the field of view  $\Omega_s = (\lambda/\Lambda)^2$  of a single-array diffraction order, and (C2)  $\omega_s = \omega_p$ . In the Fourier domain, the system's 'spatiotemporal bandwidth'  $\nu = \Omega_s \omega_s$  counts the controllable DoF per unit area and time within a single far-field diffraction order. As illustrated in Fig. 1a (shaded pillbox), (C1) and (C2) are both satisfied when  $\nu$  matches the accessible pixel bandwidth  $\Omega_p \omega_p$ .

Practical constraints have prevented present-day SLM technology from achieving this bound (Methods). Figure 1b compares the performance of various experimentally demonstrated, active 2D SLMs as a function of spatiotemporal bandwidth's two components: modulation bandwidth  $\omega_s$  and field of view  $\Omega_s$ . Controllability aside, the evident trade-off between these parameters illustrates the difficulty of creating fast, compact modulator arrays with high  $\nu$ . Thus, in addition to satisfying the complete control criteria (C1) and (C2), an 'ideal' SLM would (C3) maximize  $\nu$  by combining wavelength-scale pitches (for full-field  $\Omega_s \rightarrow 2\pi$  beamforming) with gigahertz (GHz)-order bandwidths  $\omega_s$  competitive with electronic processors; (C4) support femtojoule (fJ)-order switching energies as desired for information processing applications <sup>20</sup>; and (C5) have scalability to state-of-the-art megapixel-scale apertures.

These criteria motivate the resonant architecture shown in Fig. 1c. Here, (C3) and (C4) are achieved by switching a fully filled array of wavelength-scale resonant optical antennas with fast, fJ-order perturbations  $\Delta \epsilon_p / \epsilon \ll 1$ . Each resonator's far-field scattering and quality factor Q can then be tuned to achieve (C1) and (C2), respectively. Combined, this resonant SLM architecture enables the complete,

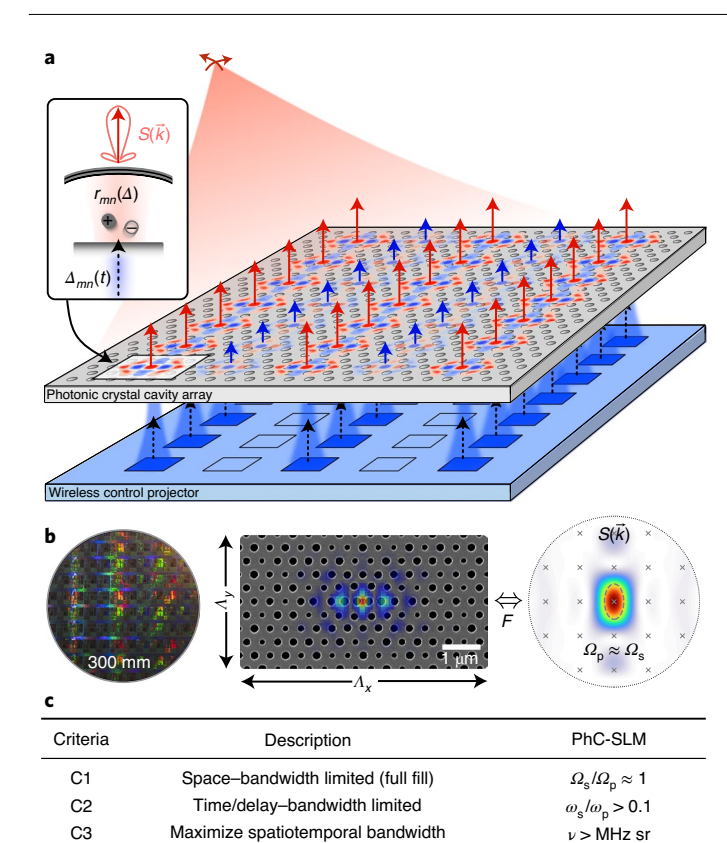
efficient control of the large spatiotemporal bandwidth supported by its constituent pixels.

Figure 2 illustrates our specific implementation of this full-DoF resonant SLM-the photonic crystal spatial light modulator (PhC-SLM)<sup>21</sup>. Coherent signal light is reflected off a semiconductor slab (permittivity ε) hosting a 2D array of semiconductor PhC cavities with instantaneous resonant frequency  $\omega_0 + \Delta_{mn}(t)$ . A short-wavelength incoherent control plane imaged onto the cavity array controls each resonator's detuning  $\Delta_{mn}(t) \approx -\Delta \epsilon(t)/2\epsilon$  via permittivity change  $\Delta \epsilon_{n}(t)$  induced by photoexcited free carriers<sup>22</sup>. We optimize the resonator bandwidth  $\Gamma \approx \omega_s \approx 2\pi \times \text{GHz}$  (corresponding to  $Q = \omega_0 / \Gamma \approx 10^5$ ) to maximize the linewidth-normalized detuning  $\Delta/\Gamma$  without substantially attenuating the cavity's response at the carrier lifetime ( $\tau$ )-limited modulation rate  $\omega_s = 1/\tau$ . By engineering the cavity's coupling regime and associated complex reflectivity  $r(\Delta)$ , the resulting linewidth-order detunings enable phase-dominant, amplitude-dominant or coupled amplitudephase modulation with negligible free-carrier absorption. Free-carrier dispersion thereby enables fast (>100 MHz given a nanosecond-order free-carrier lifetime<sup>23</sup>), low-energy (fJ-order) conversion of incoherent control light into a dense array of coherent, modulated signal modes (Supplementary Section A)<sup>24</sup>.

This out-of-plane, all-optical switching approach is motivated by the recent development of high-speed, high-brightness  $\mu LED$  arrays  $^{25,26}$  integrated with complementary metal–oxide–semiconductor (CMOS) drive electronics for consumer displays  $^{27,28}$  and high-speed visible light communication  $^{29,30}$ . In particular, gallium nitride  $\mu LED$  arrays with GHz-order modulation bandwidths  $^{30,31}$ , sub-micron pixel pitches  $^{32}$  and large pixel counts  $^{33}$  have been demonstrated within the past few years. Applying these arrays for reconfigurable, 'wireless' all-optical cavity

C4

C5



**Fig. 2** | **The PhC-SLM. a**, Complete spatiotemporal control is achieved by modulating an array of high-quality-factor  $(Q > 10^5)$ , small-mode-volume  $(V < 0.1\lambda^3)$  silicon PhC cavities with a high-speed incoherent μLED array. Absorbed μLED pulses control the detuning  $\Delta$  of resonant pixels via free-carrier dispersion, which varies the amplitude and phase (illustrated by the length and colour, respectively, of the emission arrows at each cell) of the pixel's complex reflection coefficient  $r(\Delta)$ . **b**, Despite the sub-wavelength near-field confinement (the inset shows the simulated mode profile overlaid on a scanning electron micrograph of an L4/3-type cavity<sup>58</sup>), each pixel is designed for directional  $(\Omega_p \approx \Omega_s = \lambda^2/\Lambda_x \Lambda_y)$  far-field scattering S(k) into the zeroth diffraction order ('×' symbols) to satisfy (C1). **c**, Combining the reflection from each resonant 'antenna' in a large-scale aperture fabricated via optimized 300 mm wafer-scale processing (**b**, left) enables near-ideal SLM performance per the design criteria (C1–C5).

 $E_{\text{switch}} \approx 5 \text{ fJ}$ 

300 mm wafer

fJ-order switching energy ( $E_{\text{switch}}$ )

Scalable foundry fabrication

control eliminates electronic tuning elements at each pixel to avoid optical loss, pixel-pitch limitations and interconnect bottlenecks for planar architectures (as aperture area A grows,  $\mathcal{O}(A)$  pixel controls eventually cannot be routed through the  $\mathcal{O}(\sqrt{A})$  perimeter)<sup>34</sup>.

Free of these constraints, we designed high-finesse, vertically coupled microcavities offering coupling efficiencies greater than 90%, phase-dominant reflection spectra<sup>35,36</sup> and directional emission  $(\Omega_{\rm p} \approx \Omega_{\rm s})$  for high-efficiency beamforming (the 'Inverse-designed resonant pixels' section). Bespoke, wafer-scale processing allows us to fabricate these 'resonant antennas' in arrays with mean quality factors  $\langle Q \rangle > 10^6$  and sub-nanometre-resonant-wavelength standard deviation (the 'Foundry-fabricated high-finesse microcavity arrays' section). For fine tuning, we developed a parallel laser-assisted thermal oxidation $^{37,38}$  protocol to then trim  $8 \times 8$  cavity arrays to picometre-order uniformity (the 'Holographic trimming' section), enabling high-speed spatial light modulation with fJ-order switching energies and  $\omega_s > 2\pi \times 100$  MHz (the 'All-optical spatial light modulation' section). Compared to the previous devices surveyed in Fig. 1b, our PhC-SLM offers near-complete control over an order-of-magnitude larger spatiotemporal bandwidth.

# **Inverse-designed resonant pixels**

The sub-wavelength (that is, normalized volume  $\tilde{V} = V/(\lambda/n)^3 < 1$  relative to a cubic wavelength in the confining dielectric of refractive index n), high-Q modes of 2D PhC cavities enable (C4)<sup>39</sup>, but at the expense of (C1) since Q optimization—via computationally expensive finite-difference time-domain simulations—cancels radiative leakage. Compared with the ideal apertures (Fig. 1c), these Q-optimized unit cells (that is, pixels) confine a spatially complex mode with  $\Omega_p \gg \Omega_s$  and near-zero  $\eta_0$  (Methods).

Fortunately, this limitation is not fundamental: modified hole configurations can resonantly scatter the mode's evanescent field to produce a desired far-field emission pattern. One established design is the addition of a harmonic 2a-period grating perturbation (Fig. 3a) that 'folds' energy concentrated at the band edge  $k_x = \pi/a$  back to  $k_{\parallel} = 0$ , yielding vertical radiation at the expense of reduced Q (refs.  $^{40-43}$ ). In the perturbative regime, the far-field scattering profile is an image of the broad band-edge mode. Thus, once the grating-induced loss becomes dominant, further magnifying the perturbation reduces Q without substantially improving directivity. Figure 3b shows the narrowed far-field profile produced by a grating perturbation of  $\delta r_i/r \approx 0.02$ , which balances the reduced  $Q \approx 8 \times 10^5$  with a modest diffraction efficiency improvement ( $\eta_0 = 0.18$ ; c.f.  $Q \approx \times 10^6$  and  $\eta_0 = 0.04$  for the original design shown in Extended Data Fig. 1).

By contrast, our design strategy combines semi-analytical guided-mode expansion (GME) simulations with automatic differentiation to maximize  $\eta_0$  (and therefore the effective near-field fill factor) for any given target Q using all the hole parameters (Methods). The resulting designs support tunable-Q resonances with near-diffraction-limited ( $\Omega_p \approx \Omega_s$ ) vertical beaming comparable to the ideal planar apertures of Fig. 1c. The example design shown in Fig. 3d, for instance, maintains  $Q \approx 8 \times 10^5$  with  $\eta_0 = 0.86$  based on the simulated far-field profile shown in Fig. 3e.

We prototyped each design at a commercial electron-beam lithography (EBL) foundry (Applied Nanotools) before transitioning to the wafer-scale foundry process described in the 'Foundry-fabricated high-finesse microcavity arrays' section. The near- and far-field reflection characteristics of the fabricated devices were measured with a cross-polarized microscopy setup (Methods). The results for the grating-coupled cavities are shown in Fig. 3b,c and those for the inverse-designed cavities are shown in Fig. 3e,f. The optimal grating-coupled cavities offer  $O \approx 4 \times 10^5$  at  $\lambda \approx 1.553$  nm with a near-field resonant scattering profile well centred on the cavity defect (Fig. 3c, inset). The mode mismatch between this wavelength-scale PhC mode and the wide-field input beam (Gaussian beam with an ~150 µm waist diameter for array-level excitation) is further evidenced by the small normalized reflection amplitude (relative to that of the inverse-designed cavities) on resonance as well as the broad far-field profile (Fig. 3b) with  $\eta_0 = 0.24$ .

By comparison, inverse design non-perturbatively modifies the cavity mode (Fig. 3d) to produce the near-ideal measured far-field profile of Fig. 3e satisfying (C1) with  $\eta_0$  = 0.98 while simultaneously increasing Q to 5.7 × 10<sup>5</sup>. We attribute the slight increase in the zero-order diffraction efficiency over the simulated value ( $\eta_0$  = 0.86) to the substrate-dependent effects (Supplementary Section E). The fully filled near-field resonant scattering image (Fig. 3f) explains the close resemblance between this measured  $S(\vec{k})$  and that of an ideal uniform aperture<sup>44</sup>. In addition, the narrowed emission profile yields an approximately five times increase in cross-polarized reflection and the phase-dominant simulated direct reflection spectrum (Fig. 3f). The latter is achieved by 94% one-sided coupling to a Gaussian beam with an optimized waist diameter (Supplementary Section C).

Combined, these results break the traditional coupling–Q trade-off (offering an order-of-magnitude improvement in the figure of merit  $\eta_0 \times Q$  for the prototype devices in Fig. 3) to enable high-performance beamforming at the space–bandwidth limit (C1).

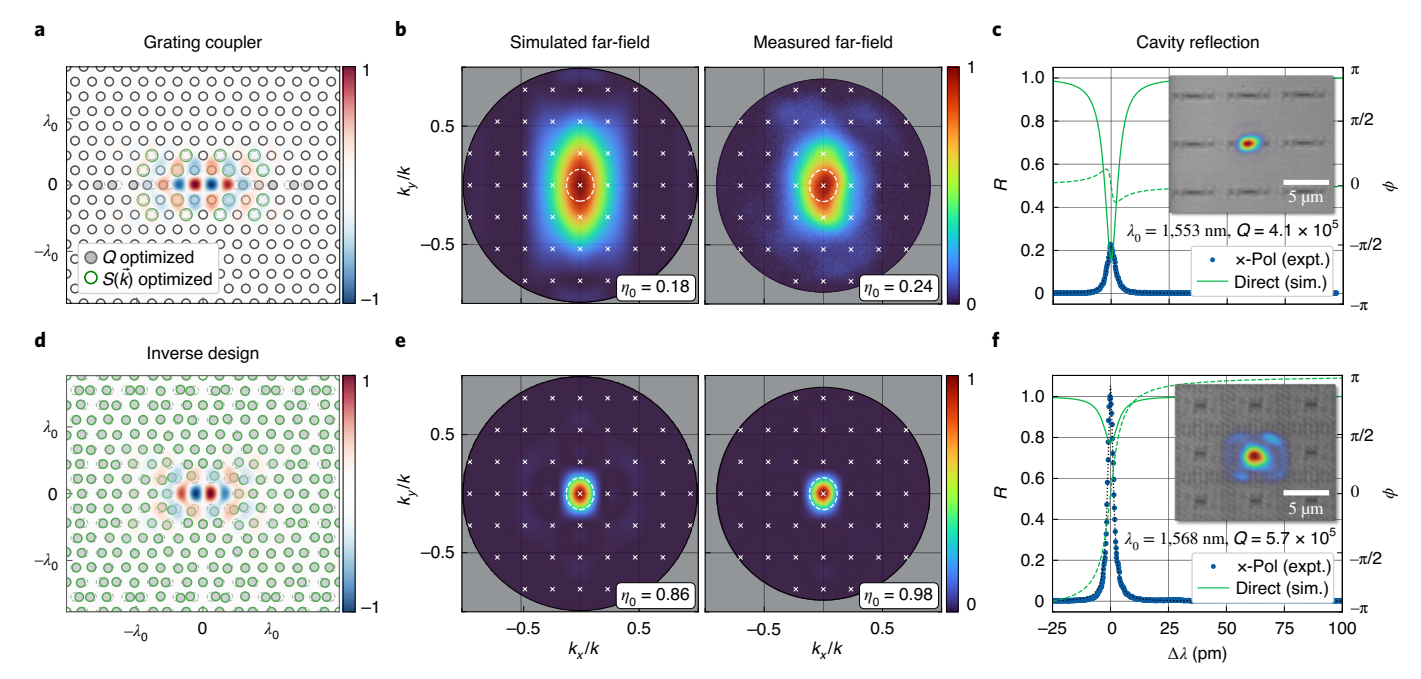


**Fig. 3** | **Conventional versus inverse-designed PhC cavities.** Superimposing a grating perturbation (green circles) on a Q-optimized L3 fundamental cavity mode (Extended Data Fig. 1) improves vertical coupling at the expense of Q ( $\mathbf{a}$ ), yielding the simulated far-field intensity profile in  $\mathbf{b}$  (left) with  $\eta_0 = 0.18$ . Hole displacements and enlargements are magnified 3 and 20 times, respectively, for visualization. Our measured far-field profile ( $\mathbf{b}$ , right) confirms the broad emission relative to the array field of view (dashed white line)  $\Omega_s$ . This mismatch explains the low effective 'fill factor' and poor coupling observed in our resonant imaging ( $\mathbf{c}$ , inset) and near-field reflection spectra ( $\mathbf{c}$ , blue), respectively. An input Gaussian beam (with waist matched to the pixel dimensions) is undercoupled

and exhibits an amplitude-dominant power reflectivity  $R = |r|^2$  modulation ( $\mathbf{c}$ , solid green) with small phase variation  $\Delta \phi$  (dashed green). Our inverse-designed cavities ( $\mathbf{d}$ ) overcome these issues by optimizing every hole in the unit cell to vertically scatter cavity leakage for any target Q, producing 'ideal' resonant SLM pixels satisfying (C1). Specifically, they support near-diffraction-limited emission ( $\mathbf{e}$ ) with  $\eta_0 \approx 1$  due to fully filled near-field resonant scattering ( $\mathbf{f}$ , inset), an approximately five times experimental resonance contrast enhancement ( $\mathbf{f}$ ), and >94% single-sided (that is, assuming the ideal back-reflector of Supplementary Section E) coupling to an input Gaussian beam for phase-dominant modulation ( $\mathbf{f}$ , green).

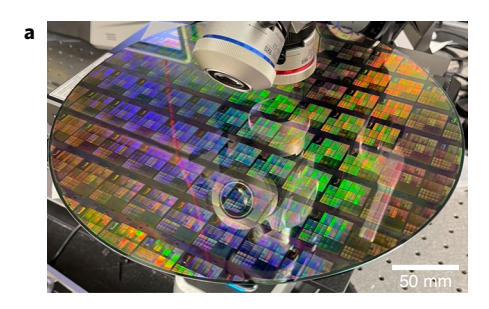
# Foundry-fabricated high-finesse microcavity arrays

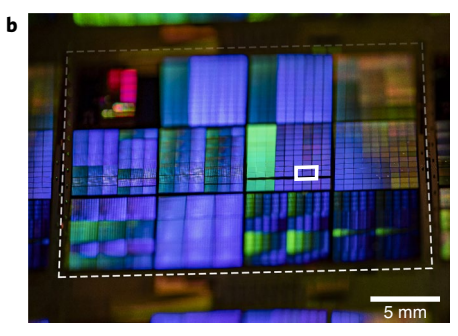
While EBL enables the fabrication of these few-pixel prototypes with state-of-the-art resolution and accuracy, serial direct-write techniques do not satisfy (C5). Field-stitching issues and sample preparation aside, a single 1 cm², megapixel-scale sample would require a full day of EBL write time alone. We therefore developed a full-wafer deep-ultraviolet photolithography process specifically optimized for wavelength-pitch arrays of high-O/VPhC microcavities in a commercial foundry <sup>45</sup>.

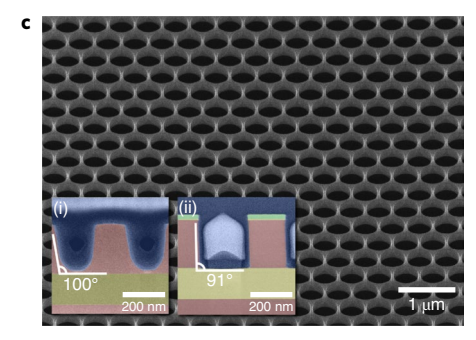
The central goal was to create vertical etch sidewalls. The transmission electron microscopy cross-section in Fig. 4(i) shows that the default fabrication process (optimized for isolated waveguides) yielded an oblique (100°), incomplete etch through the silicon device layer for the target PhC lattice parameters. Both non-idealities erase the membrane's vertical reflection symmetry, leading to coupling between even- and odd-symmetry (about the slab midplane) modes that ultimately limits the achievable Q of bandgap-confined resonances<sup>46</sup>. By contrast, our revised fabrication process achieves near-vertical 91° sidewall angles (Fig. 4(ii)), yielding high-quality PhC lattices for a range of hole diameters between the ~100 nm critical dimension and  $2r \approx a$  (Fig. 4c). Using transmission electron microscopy cross-sectioning and automated optical metrology as feedback over multiple 300 mm wafer runs in the AIM Photonics foundry's 193 nm deep-ultraviolet water-immersion lithography line, this new process relies on a combination of dose-optimized reverse-tone (positive-tone) lithography, high-accuracy laser-written masks, and optimized etch termination. Following fabrication and dicing, we post-processed individual die with a backside silicon nitride antireflection coating and, as required, suspended the PhC membranes with a timed wet etch (Supplementary Section E).

The resulting die contain isolated and arrayed PhC cavities with swept dimensions to offset systematic fabrication biases. We chose Lm-type cavity designs—formed by removing m holes from the PhC lattice as demonstrated by the L3 pixels in Fig. 3—to host tunable-volume (via variable m), high-Q resonant modes with even reflection symmetry (about the pixel axes) as required for vertical emission<sup>47</sup>. The highest-performance isolated devices feature  $Q > 10^6$  with normalized volumes  $\tilde{V} \approx 0.3$ . With a joint spectral and spatial confinement (quantified by the figure of merit  $Q/\tilde{V}$ ) of -4 × 10<sup>6</sup>, these devices are among the highest-finesse optical cavities ever fabricated in a foundry process.

Our optimized foundry processing extends this exceptional single-device performance (rivaling record EBL-fabricated devices) to large-scale cavity arrays with near-unity yield. We developed a fully automated measurement system to locate and characterize hundreds of cavities per second via parallel camera readout (Methods). The resulting data, extracted from over 105 devices measured across the wafer, allow us to statistically analyse the resonator performance and fabrication variability at the die, reticle, and wafer level. Figure 4d, for example, shows the resonant wavelength and Q variations within  $8 \times 8$ arrays of four different cavity designs. Using camera readout of the reflected wide-field excitation, each dataset is extracted from a single wavelength scan of a tunable laser. Besides the expected correlation between uniformity and mode volume<sup>48</sup>, the data demonstrate the ability to fabricate sub-wavelength ( $\tilde{V}$  < 1) microcavity arrays with  $\langle Q \rangle > 10^6$  and sub-nanometre-resonant-wavelength standard deviation  $(\sigma_{\lambda} \approx 0.6 \text{ nm})$ . Critically for beamforming, this uniformity also extends to the far field: Extended Data Fig. 4 shows that each cavity in an 8 × 8 array emits vertically with  $\eta_0 = 0.86 \pm 0.07$ , in quantitative agreement with the simulated result shown in Fig. 3.







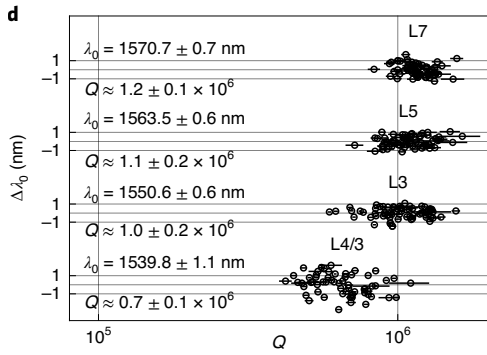


Fig. 4 | Full-wafer photonic crystal fabrication in an optimized 300 mm foundry process. A wafer (a) contains 64 complete reticles (b), each comprising millions of inverse-designed PhC cavities. The before (i) and after (ii) false-colour (blue: metal fill, red: silicon, yellow: silicon dioxide, green: etch mask) transmission electron microscopy cross-sections show how process optimization enables high-quality PhC lattices (c) that support Lm-type cavity arrays with  $\langle Q \rangle > 10^6$  and sub-nanometre-wavelength standard deviation (d).

# **Holographic trimming**

In addition to these overlapping far-field emission profiles, programmable multimode interference requires each cavity to operate near a common resonant wavelength  $\lambda_0$ . For resonators with sufficiently high Q, this tolerance cannot be solely achieved through optimized fabrication since  $\mathcal{O}(nm)$  fabrication fluctuations translate to  $\mathcal{O}(nm)$  resonant-wavelength variations  $^{49,50}$ . Our prototype  $8\times 8$  arrays of L3 cavities (chosen to optimally balance requirements on Q, V, directive emission, and fabrication tolerance) typically span an ~3 nm

peak-to-peak wavelength variation (given  $\sigma_{\lambda} \approx 0.6$  nm), corresponding to hundreds of linewidths for the target Q of ~10<sup>5</sup>.

To correct this non-uniformity, we developed an automated, low-loss and picometre-precision trimming procedure based on laser-assisted thermal oxidation (Fig. 5). Two features of our approach resolve the speed and controllability limitations of prior single-device implementations 37.38: (1) accelerated oxidation in a high-pressure chamber with in situ characterization and (2) holographic fanout of the trimming laser to simultaneously address multiple devices (Methods).

Figure 5 demonstrates the results of this trimming procedure applied to our prototype 8 × 8 pixel PhC-SLM. Before trimming, the hyperspectral near-field reflection image (Fig. 5c) shows the large (>200 linewidths for the mean quality factor  $\langle Q \rangle = 1.6 \times 10^5$ ) resonant-wavelength variation between the otherwise spatially uniform and high-fill resonant modes. Holographic trimming reduces the wavelength standard deviation and peak-to-peak spread by >100 times to  $\sigma_{\lambda} = 2.5$  pm and  $\Delta \lambda_0^{\text{p-p}} = 1.3\Gamma = 13$  pm, respectively, enabling all 64 devices (Fig. 5d) to be resonantly excited at a common operating wavelength (Fig. 5e). Since  $\sigma_{\lambda}$  is directly related to the corresponding hole radius and placement variability  $\sigma$  with an  $\mathcal{O}(1)$  design-dependent constant of proportionality, the thermal oxide homogenizes the effective dimensions of each microcavity to the picometre scale. The mean quality factor and near-field reflection profile of the array remain largely unmodified throughout the process (Fig. 5c,e).

To our knowledge, these results are the first demonstration of parallel, in situ, non-volatile microcavity trimming. The achievable scale is currently limited by environmental factors that could be overcome with stricter process control. Even without these improvements, the current uniformity, scale, and induced loss outperform the corresponding metrics of previous techniques (Extended Data Table 2), paving the way towards scalable integrated photonics with high-Q resonators.

# All-optical spatial light modulation

Once trimmed to within a linewidth, each resonator reflects an incident coherent field  $E_i(\vec{r}, t)$ , producing a far-field output<sup>51</sup>

$$E_{\rm r}(\vec{k},t) = S(\vec{k}) \sum_{m,n} r\{\Delta_{mn}(t)\} E_{\rm i}(\vec{r}_{mn},t) e^{{\rm j}\vec{k}\cdot\vec{r}_{mn}}$$
 (2)

that can be dynamically controlled within  $S(\vec{k})$  by setting the detuning  $\Delta_{mn}(t)$  (and therefore the near-field reflection coefficient r) of each resonator. Experimentally, we measure the intensity pattern  $|E_r(\vec{k})|^2$  on the back focal plane (BFP) of a microscope objective above the temperature-stabilized PhC-SLM (to enable operation without laser-cavity locking) and optically program  $\Delta_{mn}(t)$  via photoexcited free carriers (Methods).

In the absence of a control input  $(\Delta_{mn} \approx 0)$ , Fig. 6d shows the static far-field intensity pattern  $|E_r(\vec{k})|^2$  of a wide-field-illuminated,  $8\times 8$  trimmed array with  $\langle Q \rangle = 1.85\times 10^5$  and  $\sigma_\lambda = 5$  pm at  $\lambda = 1,562$  nm. The inverse-designed pixels minimize scattering into undesired diffraction orders, producing a high-efficiency ( $\eta_0 = 0.66$ ) zero-order beam with the expected  $1.3^\circ$  and  $1.6^\circ$  horizontal and vertical beamwidths, respectively, given the  $42.0\lambda \times 36.4\lambda$  aperture size. The cross-sectional beam profiles are well matched to the simulated emission profile of uniform apertures with width  $w = 0.8\lambda$ , suggesting an 80% effective linear fill of the array. This extracted value agrees with the observed zero-order efficiency and the array's physical design (each  $16a\times 16a$  cavity offering near-unity fill was padded to  $20a\times 20a$  to limit coupling to adjacent pixels).

After confirming the static performance of the array, we conducted optical switching experiments with two sources: an incoherent  $\mu LED$  array and a pulsed visible laser. The  $\mu LED$  array contains  $16\times16$  individually addressable gallium nitride  $\mu LEDs$  with >150 MHz small-signal bandwidth and -10 $^6$  cd m $^{-2}$  peak luminances (at 450 nm) flip-chip bonded to high-efficiency CMOS drivers $^{29,52}$ . Digitally

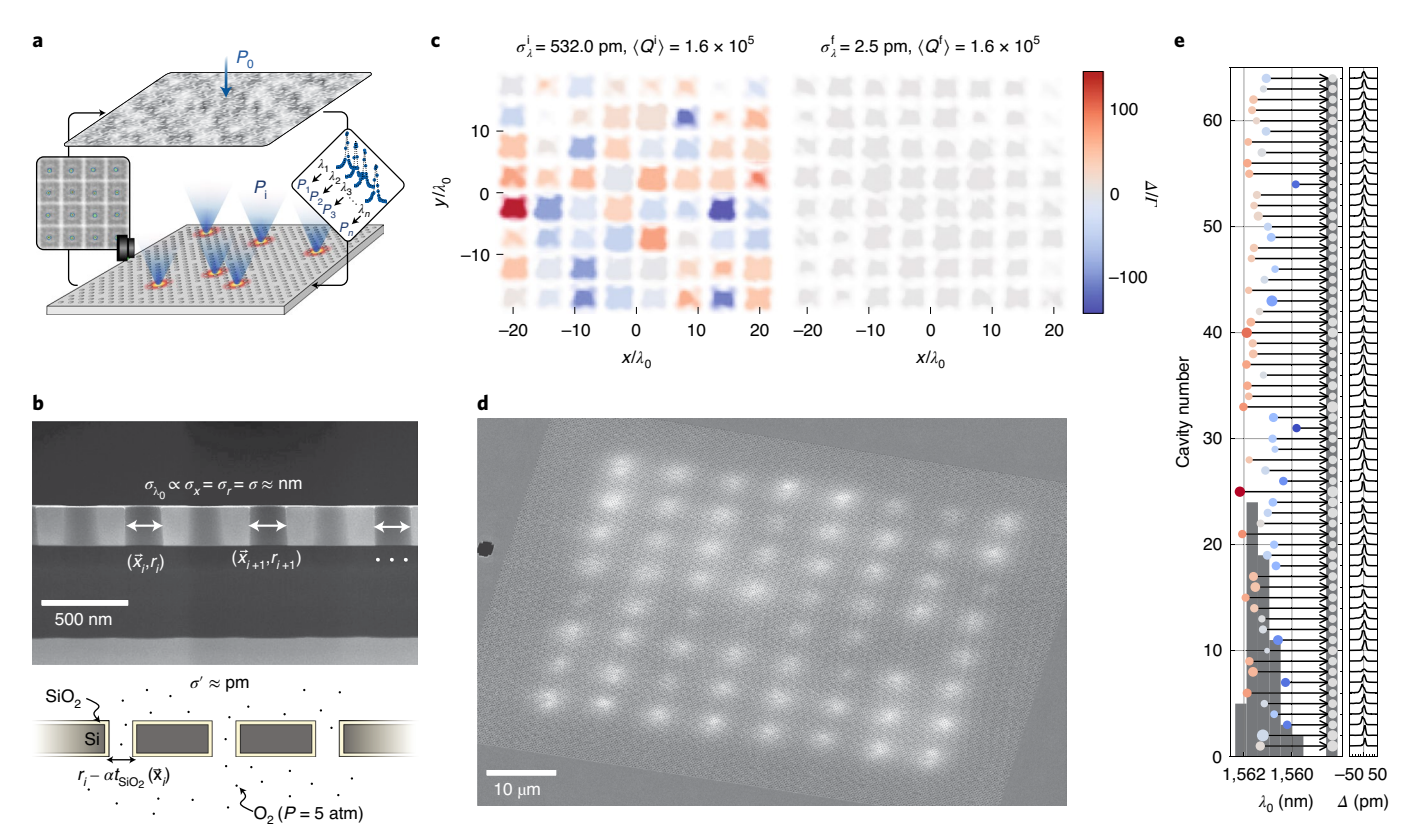


**Fig. 5** | **Parallel, fully automated and low-loss microcavity trimming via structured laser oxidation. a**, In each iteration of the trimming loop, a weighted Gerchberg–Saxton algorithm distributes a visible trimming laser with power  $P_0$  to powers  $\{P_i\}$  at the desired cavities based on the measured resonant wavelength  $\lambda_i$  of each cavity. **b**, A few-nanometre-thick layer of thermal oxide grows at each optical focus (photographed spots in the cavity array image inset), reducing the as-fabricated standard deviation in the hole parameters  $\sigma$  and permanently shifting the targeted resonances. **c**, Initial and final near-field hyperspectral

reflection images (colour coded by each device's wavelength-normalized detuning  $\Delta/I$ ) show the >100 times reduction in resonant-wavelength standard deviation to  $\sigma_{\lambda}$  = 2.5 pm without affecting the mean quality factor  $Q > 10^5$ . **d**, The effective dimensions of the final array are thus homogenized to  $\sigma' \sim$  picometre-length scales by oxidation. Regions of local oxide growth in helium-ion microscopy images of the trimmed PhC-SLM (**d**) appear as bright areas. **e**, Device summary shows the wavelength shift, Q variation (quantified by the area of the dot) and aligned reflection spectra of each device.

triggering the CMOS-controlled, 100-um-pitch array (imaged with variable demagnification and rotation onto the PhC cavity array) then enables reconfigurable, binary optical addressing as illustrated by the imaged projections of three letters on the PhC-SLM (Fig. 6a). We measured the resulting pixel reflection amplitude and phase using locked. shot-noise-limited balanced homodyne detection (Methods). Figure 6a depicts the maximum phase shift  $\Delta \phi$  as a function of CMOS trigger duration  $T_{\text{CMOS}}$  and imaged pump energy density  $E_{\text{uLED}}$ . Single-cavity switching with a maximum phase shift of  $0.3\pi$ —limited by the  $\mathcal{O}(1)$  linewidth cavity detuning produced at peak  $\mu$ LED intensity was possible with energy densities below 10 fJ  $\mu$ m<sup>-2</sup> (corresponding to ~100 fJ total energy for our chosen demagnification) and a minimum trigger duration of  $T_{\text{CMOS}} \approx 5$  ns. Shorter trigger pulses produce relatively constant-width pulses (due to the µLED fall time) with insufficient energy for high-contrast switching. Combined with the amplitudedominant cross-polarization measurement, these µLED's time dynamics (approaching those of the cavity ringdown) explain the observed deviation in switching characteristics (Fig. 3f).

Confining visible pump pulses in space and time to the silicon free-carrier diffusion length (-1  $\mu$ m) and lifetime ( $\tau \approx 1$  ns), respectively, would minimize the switching energy and maximize the bandwidth. Although either metric is achievable with existing  $\mu$ LED arrays<sup>32,53</sup> and optimization to achieve both simultaneously is ongoing<sup>54,55</sup>, we demonstrated the expected performance enhancement with a pulsed visible ( $\lambda$  = 515 nm) laser. Figure 6b shows that 3 dB power reflectivity changes and high-contrast phase modulation are feasible for 5 fJ pump

pulses over a switching interval of  $T_{\text{switch}} \approx 1 \text{ ns}$ , thereby satisfying (C4). Free-carrier dispersion is the dominant switching mechanism for these isolated, nanosecond-order switching events (Supplementary Section A). Although repeated switching over microsecond-order timescales leads to slowly varying thermo-optic detuning<sup>56</sup>, various optical communications techniques (for example, constant-duty line codes<sup>57</sup>) can maintain the average device temperature and resonant wavelength during high-speed free-carrier modulation (Supplementary Section A). To demonstrate this decoupling of switching mechanisms that enables continuous operation, we measured the normalized small-signal transfer function  $T(\omega)$  between a harmonic pump power (produced by a network-analyser-driven amplitude electro-optic modulator) and the phase-locked homodyne response. When aligned to the thermally detuned resonance, the results (Fig. 6c) match the expected second-order response  $T(\omega) = 1/\{[1 + (\omega \tau)^2]\}$  $[1 + (\omega/\pi\Gamma)^2]$  set by the carrier- and cavity-lifetime-limited bandwidths. While satisfying (C2) therefore requires higher-Q resonators, the current regime of operation enables near-complete control over a larger bandwidth  $\omega_s = 2\pi \times 135 \,\text{MHz} \approx 1/\tau$  without substantially degrading the carrier-lifetime-limited modulation bandwidth.

Combining this optimized switching with the space–bandwidth-limited vertical beaming of each resonator enables multimode programmable optics approaching the fundamental limits of spatiotemporal control. We currently probe the PhC-SLM in a wide-field, cross-polarized setup that produces amplitude-dominant Lorentzian reflection profiles  $r(\Delta) \propto 1/(1+j\Delta)$  regardless of the resonator coupling

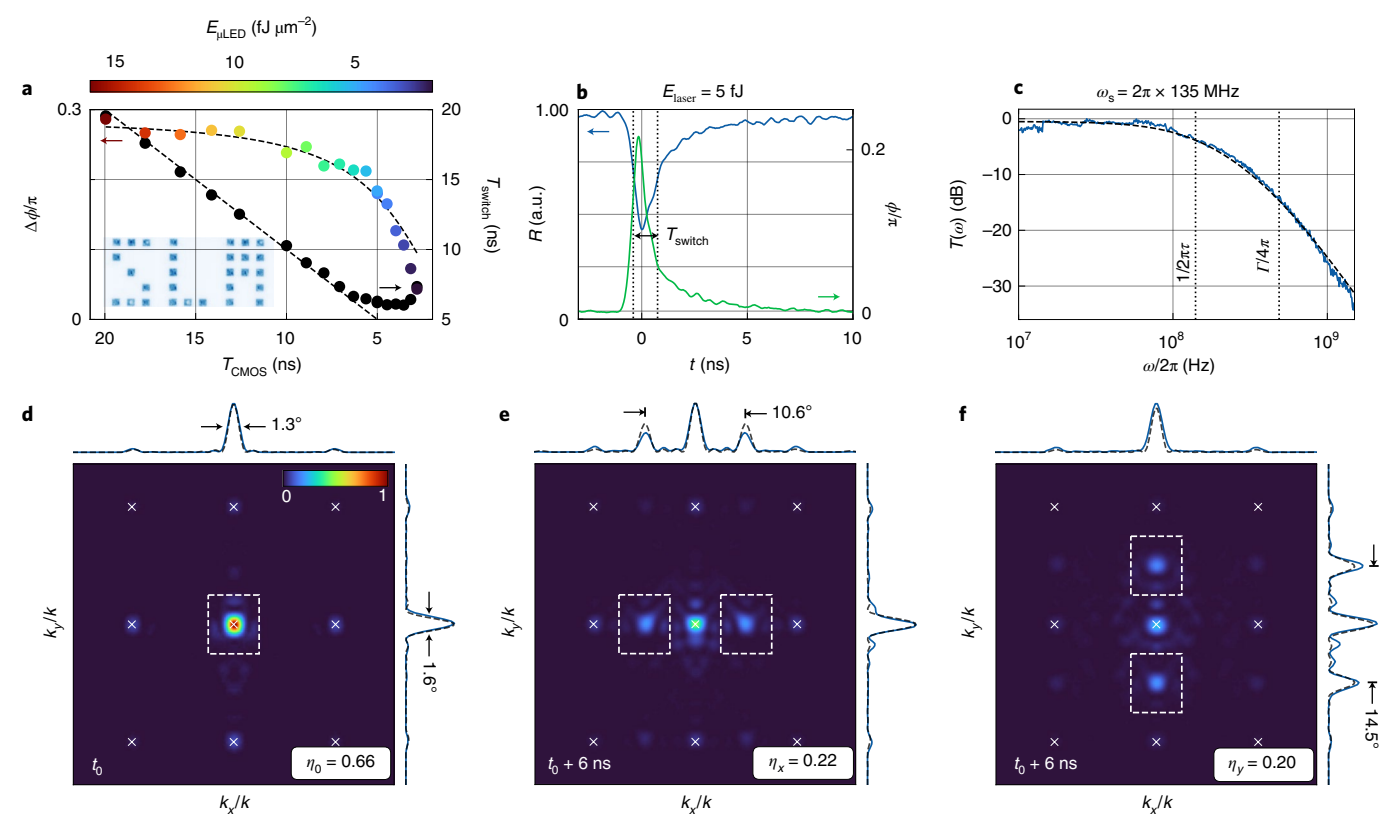


**Fig. 6** | **Nanosecond switching and spatial light modulation. a**, Peak phase shift  $\Delta \phi$  and half-maximum switching interval  $T_{\text{switch}}$  produced by pulses from a CMOS-integrated µLED array imaged onto the cavity array (the inset shows the cavities illuminated to form the letters 'S', 'L' and 'M') as a function of trigger duration  $T_{\text{CMOS}}$  and pulse energy density  $E_{\text{µLED}}$ . **b**, Complex reflectivity ( $r = \sqrt{R} \mathrm{e}^{\mathrm{i}\phi}$ ) modulation with femtojoule-order pulse energies  $E_{\text{laser}}$  from a focused visible laser. **c**, Output probe to input visible (pump) power transfer function  $T(\omega)$  fit to a second-order response function, yielding  $\omega_s = 2\pi \times 135$  MHz limited by the free carrier lifetime  $\tau \approx 1.1$  ns and cavity bandwidth  $T \approx 1$  GHz. **d**, Far-field intensity

profile, half-maximum beamwidths and zero-order diffraction efficiency  $\eta_0$  (integrated within the dashed white box) of the trimmed array at time  $t_0$  with horizontal and vertical cross-sectional profiles (blue traces) compared with those of an  $8\times 8$  array of planar apertures with 80% linear fill (black, dashed). **c.d**, Analogous results for the switched array with an optically patterned horizontal (vertical) amplitude grating at the maximum extinction time  $t_0+6$  ns, producing ±first-order diffraction peaks over a  $10.6^{\circ}$  (**e**)  $(14.5^{\circ}$  (**f**)) field of view with diffraction efficiency  $\eta_x = 0.22$  (**e**)  $(\eta_y = 0.20$  (**f**)).

regime. For simplicity, we therefore conducted proof-of-concept demonstrations using the PhC-SLM as an array of high-speed binary amplitude modulators. In this modality, a nanosecond-class pulsed visible laser is passively fanned out to the desired devices. Devices targeted by pump light are detuned far from resonance ( $\Delta \gg \Gamma$ ) and effectively extinguished, whereas unactuated cavities retain their high reflectivity at  $\Delta \approx 0$ .

We used pump-probe spectroscopy for the wide-field imaging of these few-nanosecond switching events (Methods). Figure 6e,f plots the resulting far-field intensity profiles  $|E_r|^2$  for horizontal and vertical on-off gratings. For a 5 ns probe pulse width, the maximum average near-field extinction of targeted cavities (7.4 and 9.8 dB for horizontal and vertical gratings, respectively) occurs within an ~6 ns delay, that is, just after the pump and probe pulses completely overlap. As expected, the input field is primarily scattered into first-order diffraction peaks within the (greater than  $10^{\circ}$ ) 2D field of view of S(k). The illustrated cross-sectional beam profiles again agree with the analytical results for an 80% filled linear array of uniform apertures (Fig. 6d-f, black dashed lines). For the horizontal grating (Fig. 6e), the fit is scaled by a factor of ~2 to account for the increased reflectivity of unactuated cavities during switching events, which we attribute to the residual coupling between adjacent cavities. In both cases, the pattern diffraction efficiencies—measured as the fraction of integrated power within the outlined regions in Fig.  $6-(\eta_y, \eta_y) = (0.22, 0.20)$  favourably compare with the efficiency of the fitted uniform aperture array. Even with amplitude-dominant modulation, these metrics exceed the efficiencies of previous resonator-based experiments due to our high-directivity PhC antenna array $^{35}$ .

#### **Summary and outlook**

These proof-of-concept experiments demonstrate the near-complete spatiotemporal control of a narrow-band optical field filtered in space and time by an array of wavelength-scale, high-speed resonant modulators. While the general resonant architecture (Fig. 1c) is applicable to a range of microcavity geometries and modulation schemes, our combination of high-Q, vertically coupled PhC cavities with efficient, all-optical free-carrier modulation achieves (C1-C5) with an ultrahigh per-pixel spatiotemporal bandwidth of  $v \approx 5.6$  MHz sr. This megahertz-order modulation bandwidth per aperture-limited spatial mode corresponds to a more than tenfold improvement over the 2D spatial light modulators reviewed in Fig. 1b. Our wafer-scale fabrication and parallel trimming offer a direct route towards scaling this performance to spectrally multiplexed  $\mathcal{O}(cm^2)$  apertures for a myriad of envisioned applications beyond the reach of current electronic systems (Methods), thus motivating the continued development of optical addressing and control techniques.

## **Online content**

Any methods, additional references, Nature Research reporting summaries, source data, extended data, supplementary information, acknowledgements, peer review information; details of author contributions and competing interests; and statements of

data and code availability are available at https://doi.org/10.1038/s41566-022-01086-9.

#### References

- Gardner, J. P. et al. The James Webb space telescope. Space Sci. Rev. 123, 485–606 (2006).
- Packer, A. M., Roska, B. & Häusser, M. Targeting neurons and photons for optogenetics. *Nat. Neurosci.* 16, 805–815 (2013).
- Demas, J. et al. High-speed, cortex-wide volumetric recording of neuroactivity at cellular resolution using light beads microscopy. Nat. Methods 18, 1103–1111 (2021).
- Hamerly, R., Bernstein, L., Sludds, A., Soljačić, M. & Englund, D. Large-scale optical neural networks based on photoelectric multiplication. *Phys. Rev. X* 9, 021032 (2019).
- Bogaerts, W. et al. Programmable photonic circuits. Nature 586, 207–216 (2020).
- Wetzstein, G. et al. Inference in artificial intelligence with deep optics and photonics. *Nature* 588, 39–47 (2020).
- Kok, P. et al. Linear optical quantum computing with photonic qubits. Rev. Mod. Phys. 79, 135 (2007).
- Ebadi, S. et al. Quantum phases of matter on a 256atom programmable quantum simulator. *Nature* 595, 227–232 (2021).
- Shaltout, A. M., Shalaev, V. M. & Brongersma, M. L. Spatiotemporal light control with active metasurfaces. Science 364, eaat3100 (2019).
- Li, S.-Q. et al. Phase-only transmissive spatial light modulator based on tunable dielectric metasurface. Science 364, 1087–1090 (2019).
- Zhang, X., Kwon, K., Henriksson, J., Luo, J. & Wu, M. C. A large-scale microelectromechanical-systems-based silicon photonics LiDAR. *Nature* 603, 253–258 (2022).
- Sun, J., Timurdogan, E., Yaacobi, A., Hosseini, E. S. & Watts, M. R. Large-scale nanophotonic phased array. *Nature* 493, 195–199 (2013).
- Rogers, C. et al. A universal 3D imaging sensor on a silicon photonics platform. *Nature* 590, 256–261 (2021).
- Wu, P. C. et al. Dynamic beam steering with all-dielectric electro-optic III–V multiple-quantum-well metasurfaces. Nat. Commun. 10, 3654 (2019).
- Zhang, Y. et al. Electrically reconfigurable non-volatile metasurface using low-loss optical phase-change material. Nat. Nanotechnol. 16, 661–666 (2021).
- Park, J. et al. All-solid-state spatial light modulator with independent phase and amplitude control for threedimensional LiDAR applications. *Nat. Nanotechnol.* 16, 69–76 (2021).
- Wang, Y. et al. Electrical tuning of phase-change antennas and metasurfaces. Nat. Nanotechnol. 16, 667–672 (2021).
- 18. Gabor, D. Light and information. *Prog. Opt.* **1**, 109–153 (1961).
- 19. Miller, D. A. Fundamental limit to linear one-dimensional slow light structures. *Phys. Rev. Lett.* **99**, 203903 (2007).
- Miller, D. A. Attojoule optoelectronics for low-energy information processing and communications. *J. Light. Technol.* 35, 346–396 (2017).
- 21. Panuski, C. L. & Englund, D. R. All-optical spatial light modulators. US patent 11,022,826 (2021).
- Soref, R. A. & Bennett, B. R. Electrooptical effects in silicon. *IEEE J. Quantum Electron.* 23, 123–129 (1987).
- 23. Tanabe, T., Taniyama, H. & Notomi, M. Carrier diffusion and recombination in photonic crystal nanocavity optical switches. *J. Light. Technol.* **26**, 1396–1403 (2008).
- Panuski, C., Pant, M., Heuck, M., Hamerly, R. & Englund, D. Single photon detection by cavity-assisted all-optical gain. *Phys. Rev. B* 99, 205303 (2019).

- Huang, Y., Hsiang, E.-L., Deng, M.-Y. & Wu, S.-T. Mini-LED, micro-LED and OLED displays: present status and future perspectives. *Light Sci. Appl.* 9, 105 (2020).
- Lin, J. & Jiang, H. Development of microLED. Appl. Phys. Lett. 116, 100502 (2020).
- Templier, F. et al. High-resolution active-matrix 10-µm pixel-pitch GaN LED microdisplays for augmented reality applications. In Proc. SPIE 10556, Advances in Display Technologies VIII 10556, 105560I (SPIE, 2018).
- Chen, C.-J., Chen, H.-C., Liao, J.-H., Yu, C.-J. & Wu, M.-C. Fabrication and characterization of active-matrix 960×540 blue GaN-based micro-LED display. *IEEE J. Quantum Electron.* 55, 3300106 (2019).
- Herrnsdorf, J. et al. Active-matrix GaN micro light-emitting diode display with unprecedented brightness. *IEEE Trans. Electron Devices* 62, 1918–1925 (2015).
- Ferreira, R. X. G. et al. High bandwidth GaN-based micro-LEDs for multi-Gb/s visible light communications. *IEEE Photon. Technol.* Lett. 28, 2023–2026 (2016).
- 31. Cai, Y. et al. Direct epitaxial approach to achieve a monolithic on-chip integration of a HEMT and a single micro-LED with a high-modulation bandwidth. ACS Appl. Electron. Mater. 3, 445–450 (2021).
- Park, J. et al. Electrically driven mid-submicrometre pixelation of InGaN micro-light-emitting diode displays for augmented-reality glasses. *Nat. Photon.* 15, 449–455 (2021).
- Hassan, N. B. et al. Ultra-high frame rate digital light projector using chipscale LED-on-CMOS technology. *Photonics Res.* 10, 2434–2446 (2022).
- Miller, D. A. Optical interconnects to electronic chips. Appl. Opt.
   49, F59-F70 (2010).
- 35. Horie, Y., Arbabi, A., Arbabi, E., Kamali, S. M. & Faraon, A. High-speed, phase-dominant spatial light modulation with silicon-based active resonant antennas. *ACS Photonics* **5**, 1711–1717 (2017).
- Peng, C., Hamerly, R., Soltani, M. & Englund, D. R. Design of high-speed phase-only spatial light modulators with two-dimensional tunable microcavity arrays. *Opt. Express* 27, 30669–30680 (2019).
- Lee, H. et al. Local tuning of photonic crystal nanocavity modes by laser-assisted oxidation. *Appl. Phys. Lett.* 95, 191109 (2009).
- Chen, C. J. et al. Selective tuning of high-Q silicon photonic crystal nanocavities via laser-assisted local oxidation. Opt. Express 19, 12480–12489 (2011).
- Nozaki, K. et al. Sub-femtojoule all-optical switching using a photonic-crystal nanocavity. *Nat. Photon.* 4, 477–483 (2010).
- Tran, N.-V.-Q., Combrié, S. & De Rossi, A. Directive emission from high-Q photonic crystal cavities through band folding. *Phys. Rev.* B 79, 041101 (2009).
- Tran, N.-V.-Q., Combrié, S., Colman, P., De Rossi, A. & Mei, T. Vertical high emission in photonic crystal nanocavities by band-folding design. *Phys. Rev. B* 82, 075120 (2010).
- 42. Portalupi, S. L. et al. Planar photonic crystal cavities with far-field optimization for high coupling efficiency and quality factor. *Opt. Express* **18**, 16064–16073 (2010).
- 43. Qiu, C., Chen, J., Xia, Y. & Xu, Q. Active dielectric antenna on chip for spatial light modulation. *Sci. Rep.* **2**, 855 (2012).
- 44. Hansen, R. C. Fundamental limitations in antennas. *Proc. IEEE* **69**, 170–182 (1981).
- 45. Fahrenkopf, N. M. et al. The AIM Photonics MPW: a highly accessible cutting edge technology for rapid prototyping of photonic integrated circuits. *IEEE J. Sel. Topics Quantum Electron.* **25**, 8201406 (2019).

- Asano, T., Song, B.-S. & Noda, S. Analysis of the experimental Q factors (~1 million) of photonic crystal nanocavities. Opt. Express 14, 1996–2002 (2006).
- 47. Kim, S.-H., Kim, S.-K. & Lee, Y.-H. Vertical beaming of wavelength-scale photonic crystal resonators. *Phys. Rev. B* **73**, 235117 (2006).
- Sekoguchi, H., Takahashi, Y., Asano, T. & Noda, S. Photonic crystal nanocavity with a Q-factor of ~9 million. Opt. Express 22, 916–924 (2014).
- Taguchi, Y., Takahashi, Y., Sato, Y., Asano, T. & Noda, S. Statistical studies of photonic heterostructure nanocavities with an average Q factor of three million. Opt. Express 19, 11916–11921 (2011).
- Minkov, M., Dharanipathy, U. P., Houdré, R. & Savona, V. Statistics of the disorder-induced losses of high-Q photonic crystal cavities. Opt. Express 21, 28233–28245 (2013).
- 51. Haus, H. A. Waves and fields in optoelectronics. *Prentice-Hall Series in Solid State Physical Electronics* (1984).
- 52. Zhang, S. et al. 1.5 Gbit/s multi-channel visible light communications using CMOS-controlled GaN-based LEDs. *J. Light. Technol.* **31**, 1211–1216 (2013).
- McKendry, J. J. et al. Individually addressable alingan micro-LED arrays with CMOS control and subnanosecond output pulses. *IEEE Photon. Technol. Lett.* 21, 811–813 (2009).
- 54. Lan, H.-Y. et al. High-speed integrated micro-LED array for visible light communication. Opt. Lett. **45**, 2203–2206 (2020).

- Pandey, A. & Mi, Z. III-nitride nanostructures for high efficiency micro-LEDs and ultraviolet optoelectronics. *IEEE J. Quantum Electron.* 58, 3300313 (2022).
- Barclay, P. E., Srinivasan, K. & Painter, O. Nonlinear response of silicon photonic crystal microresonators excited via an integrated waveguide and fiber taper. Opt. Express 13, 801–820 (2005).
- Winzer, P. J. & Essiambre, R.-J. Advanced modulation formats for high-capacity optical transport networks. J. Light. Technol. 24, 4711–4728 (2006).
- 58. Minkov, M., Savona, V. & Gerace, D. Photonic crystal slab cavity simultaneously optimized for ultra-high Q/V and vertical radiation coupling. *Appl. Phys. Lett.* **111**, 131104 (2017).

**Publisher's note** Springer Nature remains neutral with regard to jurisdictional claims in published maps and institutional affiliations.

Springer Nature or its licensor (e.g. a society or other partner) holds exclusive rights to this article under a publishing agreement with the author(s) or other rightsholder(s); author self-archiving of the accepted manuscript version of this article is solely governed by the terms of such publishing agreement and applicable law.

© The Author(s), under exclusive licence to Springer Nature Limited 2022, corrected publication 2023

#### Methods

#### Comparison to previous 2D SLMs

In general, commercial devices approximate design criterion (C1) without achieving (C2). Specifically, they offer excellent near-field fill factor across megapixel-scale apertures but use large  $\mathcal{O}(\varepsilon)$ , slow index perturbations. Liquid crystal SLMs, for example, are limited to  $\omega_s \approx 2\pi \times 10^3$  Hz  $\ll \omega_p$  by the slow rotation of viscous, anisotropic molecules that modulate the medium's phase delay  $^{59,60}$ . Digital micromirror-based SLMs offer moderately faster (-10 $^5$  Hz) binary amplitude modulation by displacing a mechanical reflector, but at the expense of diffraction efficiency  $^{61}$ . Mechanical phase shifters  $^{62-66}$  improve this efficiency but still require design trade-offs between pixel size and response time.

Recent research has focused on surmounting the speed limitations of commercial SLMs with integrated photonic phased arrays  $^{12,13,67,68}$  and active metasurfaces comprising thermally  $^{15,17,69}$ , mechanically or electrically  $^{14,16,71-73}$  actuated elements. These devices, however, do not satisfy (C1) (Extended Data Table 1). Silicon photonics, in particular, has attracted significant interest due to its fabrication scalability; however, the combination of standard routing waveguides, high-power (order milliwatt per  $\pi$ -phase shift) thermal phase shifters, and vertical grating couplers in each pixel reduces the fill factor of emitters, yielding  $\Omega_{\rm p} \gg \Omega_{\rm s}$  (ref.  $^{12}$ ). Scattering into the numerous diffraction orders within  $\Omega_{\rm p}$  then reduces the achievable zero-order and overall diffraction efficiencies ( $\eta_0$  and  $\eta$ , respectively). For this reason,  $\eta_0$  is a useful measure of near-field fill.

Various workarounds, including one-dimensional phased arrays with transverse-wavelength tunability  $^{67,74,75}$ , sparse antenna arrays  $^{76}$  and switched arrays  $^{11,77}$  improve the steering performance but restrict the spatiotemporal basis (that is, limit F). Alternative nanophotonics-based approaches, often limited to one-dimensional modulation, have their drawbacks as well: phase-change materials  $^{15,17,69}$  have slow crystallization rates and large switching energies, while electro-optic devices  $^{16,71-73,78-80}$ , to date, have primarily relied on large-area grating-based resonators to achieve appreciable modulation.

Extended Data Table 1 compares the PhC-SLM demonstrated here with these other actively controlled 2D SLMs (Fig. 1b). Wavelength-steered devices and switch arrays are omitted to restrict focus to the typical SLM architectures in Fig. 1. Notably, while beamsteering with PhC waveguides 77,81,82 and laser arrays 83 has recently been demonstrated, our device is the first (to our knowledge) to feature simultaneous emission from a 2D array of individually controllable PhC pixels.

# Inverse-designed photonic crystal antennas

Typical photonic crystal cavity designs—the L3 cavity shown in Extended Data Fig. 1a, for example  $^{84}$ —are designed to maximize Q by cancelling radiative leakage, yielding a broad far-field emission pattern (Extended Data Fig. 1b, background) that violates (C1) and limits the zero-order diffraction efficiency ( $\eta_0 \approx 0.04$ , in this case). The result is poor beamforming performance as exemplified by the distorted, low-efficiency far-field pattern emitted by a  $64 \times 64$  cavity array with optimized detunings (derived with the algorithm shown in Supplementary Section D) to match a target far-field image (MIT logo).

Alternatively, our inverse-design strategy (Extended Data Fig. 1b) combines semi-analytical GME simulations with efficient gradient-based optimization via automatic differentiation to enable high-quality beamforming with vertically coupled, high-Q and small-mode-volume photonic crystal microcavities. In each optimization step, GME (implemented with the open-source package legume<sup>85</sup>) approximates the cavity eigenmode and radiative loss rates  $c_{mn}^{(l)}$  at each of the array's reciprocal lattice vectors (that is, diffraction orders) offset by the Bloch periodic boundary conditions  $\vec{k}_i$  (ref. <sup>86</sup>). These coupling coefficients coarsely sample the cavity's approximate far-field emission. Scanning  $\vec{k}_i$  over the irreducible Brillouin zone of the rectangular cavity array improves the sampling resolution, and an overall Q can be

estimated by averaging the total loss rates  $\Gamma^{(i)} = \sum_{mn} c_{mn}^{(i)}$  in each simulation. Reverse-mode automatic differentiation then allows us to efficiently optimize an objective function

$$f = \frac{1}{N} \sum_{i=1}^{N} \frac{c_{00}^{(i)}}{\Gamma^{(i)}} \arctan\left(\frac{Q}{Q_0}\right) |E_0|^2$$
 (3)

targeting three main goals: (1) increase Q to a design value  $Q_0$ ; (2) force the associated radiative loss into the array's zeroth diffraction order for efficient vertical coupling; and (3) minimize V by maximizing  $|E_0|$ , the electric-field magnitude at the centre of the unit cell. Supplementary Section B further describes this technique in comparison to the existing grating coupler technique introduced in the 'Inverse-designed resonant pixels' section.

The resulting designs support high-efficiency free-space coupling (Supplementary Section C) to photonic crystal microcavities with near-unity zero-order diffraction efficiency. Combined, these features enable high-quality microcavity-based beamforming as evidenced by the simulated hologram shown in Extended Data Fig. 1d: an array of optimally detuned, inverse-designed cavities forms a clear far-field image with a several-orders-of-magnitude improvement in the overall diffraction efficiency ( $\eta$  = 0.83) over existing designs.

#### Measurement setups and techniques

Extended Data Fig. 2 illustrates the major components of our experimental setup. Here we describe the design and function of each sub-assembly.

Near-field characterization. The wide-field, cross-polarized microscope (Extended Data Fig. 2a) allows us to simultaneously measure the reflection from every cavity within a camera's field of view. A visible illumination path (not illustrated) is joined with the collimated infrared light from a tunable laser with a dichroic mirror and focused onto the BFP of an objective by lens L1. The angle of incidence and spot size of the infrared beam on the sample are therefore controlled by translating L1 and varying the collimated beam diameter, respectively. In our typical wide-field configuration, a 7.2 mm beam diameter focused to the centre of a  $\times 40$  objective's BFP yields an  $\sim 150~\mu m$  waist diameter, vertically incident field that quasi-uniformly illuminates  $10 \times 10~PhC$  cavity arrays.

By orienting the input polarization at a 45° angle relative to the dominant cavity polarization axis (with a half-wave plate or by physically rotating the sample), light coupled into and reflected by the PhC cavity is polarization rotated and can be isolated from direct, specular reflections with a polarizing beamsplitter. A kilohertz-rate free-running, dual-band (visible and infrared) camera images this cross-polarized reflection signal through tube lens L3. For each frame collected during a laser sweep, the wavelength is interpolated from the recorded camera and laser output triggers, and each cavity's reflection is integrated over a fraction of pixels within its imaged unit-cell boundary. We use the resulting high-contrast reflection spectra (across all the devices within the field of view) to characterize the device performance and monitor the cavity trimming process. The sample mount below the objective (OL) is temperature stabilized to within 10 mK with a Peltier plate and feedback controller. For trimming experiments, the sample is placed in a high-pressure oxygen environment within a custom chamber offering in situ optical access through a glass window.

**Calibrated far-field measurement.** Inserting a lens (L2) in the collection path one focal length from the objective BFP allows us to measure the far-field profile  $S(\vec{k})$  of individual or multiple cavities using the same setup. We position an iris at the intermediate image plane—located with a removable lens (not shown) placed before L3—to spatially filter the emission from the desired devices. We also calibrate the BFP scale using a reflective reference grating with a known pitch. Due to the cross-polarized configuration, only a single polarization  $\tilde{S}(\vec{k})|_{\theta}$  is

imaged for any cavity-input polarization angle difference  $\theta$ . The complete cavity emission profile

$$S(\vec{k}) = \tilde{S}(\vec{k})|_{\theta} + \tilde{S}(\vec{k})|_{\theta + \pi/2} \tag{4}$$

can therefore be reconstructed by sequentially imaging both polarizations (as shown in Extended Data Fig. 3a–c for  $\theta$ =  $45^{\circ}$ ). For maximum accuracy, we used this technique for the experimental results shown in Fig. 3.

Alternatively, the specific choice of  $\theta$  = 45° allows  $S(\vec{k})$  to be reconstructed from a single measurement. Due to mirror symmetry about the cavity's principal polarization axis  $\hat{y}$ , Extended Data Fig. 3a,b shows that  $\hat{\sigma}_{\hat{y}}\{\tilde{S}(\vec{k})|_{\pm 45^{\circ}}\} = \tilde{S}(\vec{k})|_{\mp 45}$  for the reflection operator  $\hat{\sigma}$ . This alternative reconstruction

$$S(\vec{k}) = [1 + \hat{\sigma}_{\hat{v}}] S(\vec{k})|_{+45^{\circ}}$$
 (5)

is experimentally demonstrated in Fig. 3d, yielding excellent agreement with Fig. 3c.

This technique simplifies high-throughput far-field measurements across cavity arrays. In Extended Data Fig. 4, for example, we used this approach to demonstrate the far-field uniformity characteristic of inverse-designed and grating-coupled L3 cavity arrays. Averaged across the  $8\times 8$  arrays, the former offers an approximately three times improvement in zero-order diffraction and aperture efficiencies  $(\langle \eta_0 \rangle = 0.86$  and  $\langle \eta_a \rangle = 0.99$ , respectively).

Pump-probe spectroscopy. Wide-field, time-resolved near- and far-field measurements can also be collected using the setup shown in Extended Data Fig. 2a via pump-probe spectroscopy. For these measurements, short infrared probe pulses were carved (with an electro-optic amplitude modulator that was d.c. biased to an intensity null) and variably delayed to coincide with the arrival of visible pump light at the PhC membrane, thereby gating the probe field transmission to the infrared camera. We then measured the near- and far-field reflection as a function of the probe delay to reconstruct switching events with sub-nanosecond resolution. The minimum probe pulse width (-5 ns) used to collect the data in Fig. 6e,f was limited by the requirement for high imaging contrast between probe pulses and leakage (due to the imperfect probe modulator extinction) given the instrument-limited trigger repetition rate (order megahertz) and camera integration time.

**Homodyne measurement.** The shot-noise-limited balanced homodyne detection setup in Extended Data Fig. 2c enables complex reflection coefficient measurements with greater than 3 dB shot-noise clearance below 1 GHz (ref.  $^{87}$ ). Signal light reflected from the cavity combines with a path-length-matched (to within millimetres based on time-delay measurements with a picosecond-class pulsed laser) local oscillator (LO), and both signals are coupled into a balanced detector using antireflection-coated fibres. The in-phase (I(t)) and quadrature (Q(t)) components of the cavity reflection were sequentially measured by locking to the first and second harmonics of the balanced output in the presence of a piezo-driven local-oscillator phase dither. The resonant, cross-polarized cavity reflection R and phase shift  $\phi$  are then reconstructed as

$$R = \frac{\left[V_{\rm p} - I(t)\right]^2 + Q^2(t)}{V_{\rm p}^2} \text{ and } \phi = \arctan \frac{Q(t)}{V_{\rm p} - I(t)}$$
 (6)

by normalizing to the measured peak voltage swing  $V_{\rm p}$  of the interference signal.

**Parallel cavity trimming.** A liquid-crystal-on-silicon (LCOS) SLM (Extended Data Fig. 2c) actively distributes a high-power continuous-wave visible laser to the target devices during the cavity

trimming procedure. The input laser was tunably attenuated with a motorized half-wave plate (preceding a PBS) and subsequently expanded to overfill the LCOS aperture. The LCOS SLM was re-imaged onto the objective BFP (as confirmed by imaging with L2 in place) using two lenses (L4 and L5) with focal lengths chosen to optimally match the imaged SLM and objective pupil dimensions. Phase-retrieval-computed holograms then evenly distribute power to an array of focused spots on the sample (Supplementary Section F) when the mechanical shutter (a flip mirror) is opened.

**μLED imaging.** The collection optics shown in Extended Data Fig. 2d maximize the intensity of a μLED array projected onto the PhC membrane within the constraints dictated by the constant radiance theorem of incoherent imaging. Assuming a Lambertian emission profile, geometric optics gives the collection efficiency  $\eta_c = \alpha_c^2$  for an objective lens (CL) with numerical aperture  $\alpha_c$  focused on the μLED array. The projection efficiency  $\eta_p$  through the projection objective (OL, with numerical aperture  $\alpha_p$ ) depends on the relative pupil sizes of both objectives and can be similarly approximated from geometric optics. The resulting intensity enhancement  $\zeta = \eta_c \eta_p / M^2$  between the source and image (with magnification M) reaches a maximum  $\zeta_{\text{max}} = \frac{1}{M^2 + (1 - \alpha_0^2)/\alpha_0^2}$ 

when the CL-collimated light overfills the back aperture of OL. The resulting design criterion

$$\alpha_{\rm c} > \sqrt{\frac{M^2 \alpha_{\rm p}^2}{(M^2 - 1)\alpha_{\rm p}^2 + 1}},$$
(7)

is achieved for our imaging setup with  $\alpha_c = 0.25$ ,  $\alpha_p = 0.95$ , and  $M \approx 1/30$ . After CL, the overall magnification and rotation are fine-tuned with a variable beam expander and Dove prism, respectively.

#### **Holographic trimming**

In each iteration of the automated trimming loop (Fig. 5a), the resonant wavelengths  $\{\lambda_i\}$  are measured and a subset T containing N devices is selected to maximize the total trimming distance  $N(\min\{\lambda_i\} - \lambda_t)$  to a target wavelength  $\lambda_t$ . Each cavity in T is then targeted by a visible laser distributed by the liquid-crystal SLM setup (Extended Data Fig. 2c). To generate the required phase masks, we developed an open-source, GPU-accelerated experimental holography software package that implements fixed-phase, weighted Gerchberg–Saxton phase retrieval algorithms. Using camera feedback, the algorithm can generate thousands of near-diffraction-limited foci with -1% peak-to-peak power uniformity and single-camera-pixel-order location accuracy within a few iterations (Supplementary Section F).

The holographically targeted pixels are then laser-heated with a computed exposure power and duration (based on the current trimming rates, resonance locations, and other array characteristics) to grow thermal oxide at the membrane surface. For thin oxide layers, the consumption of silicon during the reaction with ambient oxygen permanently blueshifts the cavity resonance in proportion to the oxide thickness  $t_{SiO_2}$  (Fig. 5b)<sup>38</sup>. Per the Deal–Grove model, the rate-limiting diffusion of oxygen through the grown oxide accelerates with increasing oxygen pressure-a well-known technique in microelectronics fabrication<sup>88</sup>. We therefore oxidize our samples in pure oxygen with partial pressure  $P_{0} = 5$  bar, enabling  $d\lambda_0/dt \approx 0.1$  nm s<sup>-1</sup> resonance trimming rates over wavelength ranges  $\Delta \lambda_0 > 20$  nm. After each trimming exposure, we remeasure the resonance statistics and recycle the loop until all the devices are aligned within a set tolerance about  $\lambda_t$ . The trimming algorithm also accounts for long-term moisture adsorption to the membrane surface, thermal crosstalk and trimming rate variations.

Figure 5 schematically outlines this trimming procedure. The main loop consists of device selection, hologram setup, parallel laser oxidation and resting intervals. The algorithm monitors two resonant

wavelengths: the instantaneous wavelength  $\lambda_i$  and the steady-state wavelength  $\lambda_0$ . Initially,  $\lambda_i = \lambda_0$ ; however, focusing high-power (-10 mW) visible light onto the cavity (as required to sufficiently heat the PhC membrane for thermal oxidation) causes a temporary blueshift  $\Delta\lambda_0$  due to the desorption of moisture attached to hydrophilic hydroxyl surface terminations. For any target rest wavelength  $\lambda_t$ , we therefore trim devices to an instantaneous wavelength  $\lambda_i = \lambda_t - \Delta\lambda_0$  that relaxes over  $\mathcal{O}(\text{min})$  timescales to  $\lambda_i = \lambda_0 = \lambda_t$  as moisture re-adsorbs to the surface. In practice, the stability and estimation of the 'overtune'  $\Delta\lambda_0$  limit the uniformity and scale of the trimming process, respectively.

After initializing the cavity locations, scanning the device resonances, and calibrating the SLM (Supplementary Section F), a spot array targeting every cavity (as shown in Extended Data Fig. 6, for example) is projected onto the membrane for a short duration (few seconds). Monitoring the resonances at fixed intervals  $\Delta t \approx 10$  s until  $\lambda_i$  stabilizes to the rest wavelength  $\lambda_0$  gives an initial estimate  $\Delta \lambda_0 = \lambda_0$  – min{\$\lambda\_i\$} for the overtune parameter of each cavity. We also update the target wavelength  $\lambda_t = \min\{\lambda_0\}$  and rest wavelengths before continuing the trimming procedure. To update  $\Delta \lambda_0$ , we periodically conduct this same 'rest loop' when  $\lambda_0$  of each cavity is below an algorithmically chosen 'checkpoint' wavelength  $\lambda_{\rm rest}$ .

As described in the 'Holographic trimming' section, a subset of N cavities is then selected to maximize the total possible trimming distance to  $\lambda_{\rm t}$ . The number of targeted cavities neighbouring each untargeted cavity is also limited to reduce crosstalk. A spot array is then formed to evenly distribute the trimming laser to the selected devices. After confirming that the location accuracy and power uniformity of the array are within tolerance, we alternate the exposure and readout intervals to grow thermal oxide with in situ monitoring. The laser power is progressively increased to reach a desired wavelength-uniformity-dependent trimming rate. As evidenced by Supplementary Fig. 8, the rate is relatively power independent until reaching a threshold power. We detect and save these threshold powers for use when selecting the initial exposure power in each trimming loop.

The trimming sub-loop continues until the estimated  $\lambda_0$  of any targeted cavity crosses  $\lambda_t$ . New cavities are then selected, targeted and trimmed until a rest period is triggered. When the peak-to-peak wavelength uniformity at the end of a rest period is below the user-defined tolerance  $\lambda_{\text{tol}}$ , the process is terminated. Extended Data Table 2 compares the demonstrated performance with other arrayed microcavity trimming techniques.

#### **Envisioned applications**

The PhC-SLM opens the door to a number of applications and opportunities including the following: 'high-definition, high-frame-rate holographic displays' by the integration of a back-reflector (Supplementary Sections C-E) for one-sided, phase-only and full-DoF spatiotemporal modulation; 'compact device integration' via direct transfer printing of our cavity arrays onto a high-bandwidth µLED array<sup>89</sup>; 'three-dimensional optical addressing and imaging' by combining on-demand µLED control with statically trimmed detuning profiles that continuously steer pre-programmed patterns<sup>90</sup>; 'large-scale programmable unitary transformations' for universal linear optics processors<sup>5</sup> enabled by overcoupled PhC reflectors; 'focal plane array sensors' for high-spatial-resolution readout of refractive index perturbations in imaging applications from endoscopy to bolometry and quantum-limited super-resolution 91-93; optical neural network acceleration' via low-power, high-density unitary transformation of free-space optical inputs<sup>4,6</sup>; and 'high-speed adaptive optics' enabling free-space compressive sensing, deep-brain neural stimulation and real-time scattering matrix inversion in complex media 94,95. Moreover, whereas we have so far considered only mode transformations, the PhC-SLM's high-Q/V resonant enhancement suggests the possibility of programming the quantum-optical excitations/fields of these modes for applications ranging from multimode squeezed light generation 96

to multiplexed single-photon sources for linear-optics quantum computing  $^{7.97}$  or deterministic photonic logic  $^{98,99}$ .

## Data availability

The main data supporting the findings of this study are available within the Article and its Supplementary Information. Additional data are available from the corresponding authors upon reasonable request.

# **Code availability**

The SLM control and holography software developed for this study is available online via GitHub at https://github.com/QPG-MIT/slmsuite. A sample finite-difference time-domain simulation is available at https://www.flexcompute.com/userprojects/a-full-degree-of-freedom-spatiotemporal-light-modulator. All the other algorithms are documented within the Article and its Supplementary Information.

#### References

- Heilmeier, G. H., Zanoni, L. A. & Barton, L. A. Dynamic scattering: a new electrooptic effect in certain classes of nematic liquid crystals. *Proc. IEEE* 56, 1162–1171 (1968).
- Zhang, Z., You, Z. & Chu, D. Fundamentals of phase-only liquid crystal on silicon (LCOS) devices. *Light Sci. Appl.* 3, e213 (2014).
- 61. Ren, Y.-X., Lu, R.-D. & Gong, L. Tailoring light with a digital micromirror device. *Ann. Phys.* **527**, 447–470 (2015).
- Hornbeck, L. J. 128×128 deformable mirror device. *IEEE Trans. Electron Devices* 30, 539–545 (1983).
- 63. Greenlee, C. et al. Electro-optic polymer spatial light modulator based on a Fabry–Perot interferometer configuration. *Opt. Express* **19**, 12750–12758 (2011).
- Yang, W. et al. High speed optical phased array using high contrast grating all-pass filters. Opt. Express 22, 20038–20044 (2014).
- 65. Wang, Y. et al. 2D broadband beamsteering with large-scale MEMS optical phased array. Optica **6**, 557–562 (2019).
- Tzang, O. et al. Wavefront shaping in complex media with a 350 kHz modulator via a 1D-to-2D transform. *Nat. Photon.* 13, 788–793 (2019).
- Chung, S., Abediasl, H. & Hashemi, H. A monolithically integrated large-scale optical phased array in silicon-on-insulator CMOS. *IEEE J. Solid-State Circuits* 53, 275–296 (2017).
- 68. Poulton, C. V. et al. Long-range LiDAR and free-space data communication with high-performance optical phased arrays. *IEEE J. Sel. Topics Quantum Electron.* **25**, 7700108 (2019).
- Wang, Q. et al. Optically reconfigurable metasurfaces and photonic devices based on phase change materials. *Nat. Photon.* 10, 60–65 (2016).
- 70. Arbabi, E. et al. MEMS-tunable dielectric metasurface lens. *Nat. Commun.* **9**, 812 (2018).
- Smolyaninov, A., El Amili, A., Vallini, F., Pappert, S. & Fainman, Y. Programmable plasmonic phase modulation of free-space wavefronts at gigahertz rates. *Nat. Photon.* 13, 431–435 (2019).
- 72. Shirmanesh, G. K., Sokhoyan, R., Wu, P. C. & Atwater, H. A. Electro-optically tunable multifunctional metasurfaces. *ACS Nano* **14**, 6912–6920 (2020).
- Benea-Chelmus, I.-C. et al. Electro-optic spatial light modulator from an engineered organic layer. *Nat. Commun.* 12, 5928 (2021).
- 74. Kim, T. et al. A single-chip optical phased array in a wafer-scale silicon photonics/CMOS 3D-integration platform. *IEEE J. Solid-State Circuits* **54**, 3061–3074 (2019).
- Poulton, C. V. et al. 8192-element optical phased array with 100° steering range and flip-chip CMOS. In Conference on Lasers and Electro-Optics, OSA Technical Digest JTh4A.3 (Optical Society of America, 2020).

- Fatemi, R., Khachaturian, A. & Hajimiri, A. A nonuniform sparse 2D large-FOV optical phased array with a low-power PWM drive. *IEEE J. Solid-State Circuits* 54, 1200–1215 (2019).
- 77. Ito, H. et al. Wide beam steering by slow-light waveguide gratings and a prism lens. *Optica* **7**, 47–52 (2020).
- 78. Huang, Y.-W. et al. Gate-tunable conducting oxide metasurfaces. *Nano Lett.* **16**, 5319–5325 (2016).
- Shuai, Y.-C. et al. Coupled bilayer photonic crystal slab electro-optic spatial light modulators. *IEEE Photon. J.* 9, 7101411 (2017).
- 80. Ye, X. et al. High-speed programmable lithium niobate thin film spatial light modulator. *Opt. Letters* **46**, 1037–1040 (2021).
- 81. Vercruysse, D., Sapra, N. V., Yang, K. Y. & Vuckovic, J. Inverse-designed photonic crystal circuits for optical beam steering. ACS Photonics **8**, 3085–3093 (2021).
- 82. Tamanuki, T., Ito, H. & Baba, T. Thermo-optic beam scanner employing silicon photonic crystal slow-light waveguides. *J. Light. Technol.* **39**, 904–911 (2021).
- 83. Sakata, R. et al. Dually modulated photonic crystals enabling high-power high-beam-quality two-dimensional beam scanning lasers. *Nat. Commun.* **11**, 3487 (2020).
- 84. Minkov, M. & Savona, V. Automated optimization of photonic crystal slab cavities. *Sci. Rep.* **4**, 5124 (2014).
- Minkov, M. et al. Inverse design of photonic crystals through automatic differentiation. ACS Photonics 7, 1729–1741 (2020).
- Andreani, L. C. & Gerace, D. Photonic-crystal slabs with a triangular lattice of triangular holes investigated using a guided-mode expansion method. *Phys. Rev. B* 73, 235114 (2006).
- 87. Panuski, C., Englund, D. & Hamerly, R. Fundamental thermal noise limits for optical microcavities. *Phys. Rev. X* **10**, O41046 (2020).
- 88. Lie, L. N., Razouk, R. R. & Deal, B. E. High pressure oxidation of silicon in dry oxygen. *J. Electrochem*. Soc. **129**, 2828 (1982).
- 89. Carreira, J. et al. Gigabit per second visible light communication based on AlGaInP red micro-LED micro-transfer printed onto diamond and glass. *Opt. Express* **28**, 12149–12156 (2020).
- Shaltout, A. M. et al. Spatiotemporal light control with frequency-gradient metasurfaces. Science 365, 374–377 (2019).
- 91. Pahlevaninezhad, H. et al. Nano-optic endoscope for high-resolution optical coherence tomography in vivo. *Nat. Photon.* **12**, 540–547 (2018).
- 92. Watts, M. R., Shaw, M. J. & Nielson, G. N. Microphotonic thermal imaging. *Nat. Photon.* **1**, 632–634 (2007).
- 93. Grace, M. R., Dutton, Z., Ashok, A. & Guha, S. Approaching quantum-limited imaging resolution without prior knowledge of the object location. *J. Opt. Soc. Am. A* **37**, 1288–1299 (2020).
- 94. Mosk, A. P., Lagendijk, A., Lerosey, G. & Fink, M. Controlling waves in space and time for imaging and focusing in complex media. *Nat. Photon.* **6**, 283–292 (2012).
- Yoon, S. et al. Deep optical imaging within complex scattering media. Nat. Rev. Phys. 2, 141–158 (2020).
- Bourassa, J. E. et al. Blueprint for a scalable photonic fault-tolerant quantum computer. Quantum 5, 392 (2021).
- 97. Bartolucci, S. et al. Fusion-based quantum computation. Preprint at https://arxiv.org/abs/2101.09310 (2021).
- 98. Heuck, M., Jacobs, K. & Englund, D. R. Controlled-phase gate using dynamically coupled cavities and optical nonlinearities. *Phys. Rev. Lett.* **124**, 160501 (2020).
- 99. Krastanov, S. et al. Room-temperature photonic logical qubits via second-order nonlinearities. *Nat. Commun.* **12**, 191 (2021).
- 100. Dostart, N. et al. Serpentine optical phased arrays for scalable integrated photonic lidar beam steering. Optica 7, 726–733 (2020).
- Aflatouni, F., Abiri, B., Rekhi, A. & Hajimiri, A. Nanophotonic projection system. Opt. Express 23, 21012–21022 (2015).

- Junique, S. et al. GaAs-based multiple-quantum-well spatial light modulators fabricated by a wafer-scale process. Appl. Opt. 44, 1635–1641 (2005).
- 103. Yaacobi, A. et al. Integrated phased array for wide-angle beam steering. *Opt. Lett.* **39**, 4575–4578 (2014).
- 104. Bartlett, T. A., McDonald, W. C. & Hall, J. N. Adapting Texas Instruments DLP technology to demonstrate a phase spatial light modulator. In Proc. SPIE 10932, Emerging Digital Micromirror Device Based Systems and Applications XI 10932, 109320S (SPIE, 2019).
- 105. Shrauger, V. & Warde, C. Development of a high-speed high-fill-factor phase-only spatial light modulator. In Proc. SPIE 4291, Diffractive and Holographic Technologies for Integrated Photonic Systems 4291, 101–108 (SPIE, 2001).
- 106. Li, J., Yu, P., Zhang, S. & Liu, N. Electrically-controlled digital metasurface device for light projection displays. *Nat. Commun.* 11, 3574 (2020).
- 107. Marshel, J. H. et al. Cortical layer-specific critical dynamics triggering perception. Science **365**, eaaw5202 (2019).
- 108. McKnight, D. J., Johnson, K. M. & Serati, R. A. 256×256 liquid-crystalon-silicon spatial light modulator. *Appl. Opt.* **33**, 2775–2784 (1994).
- 109. Jayatilleka, H. et al. Post-fabrication trimming of silicon photonic ring resonators at wafer-scale. J. Light. Technol. 39, 5083–5088 (2021).
- Biryukova, V., Sharp, G. J., Klitis, C. & Sorel, M. Trimming of silicon-on-insulator ring-resonators via localized laser annealing. Opt. Express 28, 11156–11164 (2020).
- 111. Hagan, D. E., Torres-Kulik, B. & Knights, A. P. Post-fabrication trimming of silicon ring resonators via integrated annealing. *IEEE Photon. Technol. Lett.* **31**, 1373–1376 (2019).
- 112. Han, S. & Shi, Y. Post-fabrication trimming of photonic crystal nanobeam cavities by electron beam irradiation. *Opt. Express* **26**, 15908–15913 (2018).
- Gil-Santos, E. et al. Scalable high-precision tuning of photonic resonators by resonant cavity-enhanced photoelectrochemical etching. Nat. Commun. 8, 14267 (2017).
- Spector, S., Knecht, J. M. & Juodawlkis, P. W. Localized in situ cladding annealing for post-fabrication trimming of silicon photonic integrated circuits. *Opt. Express* 24, 5996–6003 (2016).
- 115. Lipka, T., Kiepsch, M., Trieu, H. K. & Müller, J. Hydrogenated amorphous silicon photonic device trimming by UV-irradiation. *Opt. Express* **22**, 12122–12132 (2014).
- Atabaki, A. H., Eftekhar, A. A., Askari, M. & Adibi, A. Accurate post-fabrication trimming of ultra-compact resonators on silicon. Opt. Express 21, 14139–14145 (2013).
- 117. Cai, T., Bose, R., Solomon, G. S. & Waks, E. Controlled coupling of photonic crystal cavities using photochromic tuning. *Appl. Phys. Lett.* **102**, 141118 (2013).
- Hennessy, K., Högerle, C., Hu, E., Badolato, A. & Imamoğlu,
   A. Tuning photonic nanocavities by atomic force microscope nano-oxidation. *Appl. Phys. Lett.* 89, 041118 (2006).

#### **Acknowledgements**

We thank the MITRE Quantum Moonshot Program for program oversight, Flexcompute for supporting finite-difference time-domain simulations, the MIT.nano staff for fabrication assistance, and M. ElKabbash (MIT) for useful discussions. C.L.P. was supported by the Hertz Foundation Elizabeth and Stephen Fantone Family Fellowship. I.C. was supported by the National Defense Science and Engineering Graduate Fellowship Program and the National Science Foundation (NSF) award DMR-1747426. S.T.-M. is funded by the Schmidt Postdoctoral Award and the Israeli Vatat Scholarship. Experiments were supported in part by Army Research Office grant W911NF-20-1-0084 (D.R.E.), supervised by M. Gerhold; the Air Force Research Laboratory under agreements FA8650-21-2-1000 and FA8750-21-2-0004; the Engineering and Physical Sciences Research

Council grants EP/M01326X/1 and EP/T00097X/1 (M.D.D. and M.J.S.); and the Royal Academy of Engineering Research Chairs and Senior Research Fellowships (M.J.S.). This material is based on the research sponsored by the Air Force Research Laboratory under agreement no. FA8650-21-2-1000. The US Government is authorized to reproduce and distribute reprints for governmental purposes notwithstanding any copyright notation thereon. The views and conclusions contained herein are those of the authors and should not be interpreted as necessarily representing the official policies or endorsements, either expressed or implied, of the United States Air Force, the Air Force Research Laboratory or the US Government.

# **Author contributions**

C.L.P. and D.R.E. conceived the idea, developed the theory and led the research. M.M. and C.L.P. developed the far-field optimization technique and designs. C.J.B. developed the optimized the resonator detuning theory. C.L.P. conducted the experiments with assistance from I.C. (trimming experiments), S.T.-M. (holography software) and A.D.G. (µLED measurements). J.J.D.M., M.D.D. and M.J.S. contributed the µLED arrays and guided the incoherent switching experiments. C.H. and J.N.W.-B. fabricated the initial samples for evaluation before foundry process development by C.T., J.S.L., J.M. and G.L.L. S.F.P. assisted with the wafer post-processing. M.L.F. coordinated and led the foundry fabrication with assistance from G.L.L. and D.J.C. C.L.P. wrote the manuscript with input from all the authors.

# **Competing interests**

C.L.P. and D.R.E. are authors of US patent 11,022,826 (all-optical spatial light modulators) and US patent App. 16/876,477 (high-speed wavelength-scale spatial light modulators with two-dimensional tunable microcavity arrays) that outline the all-optical control scheme and resonant architecture of the PhC-SLM developed here. The other authors declare no competing interests.

#### **Additional information**

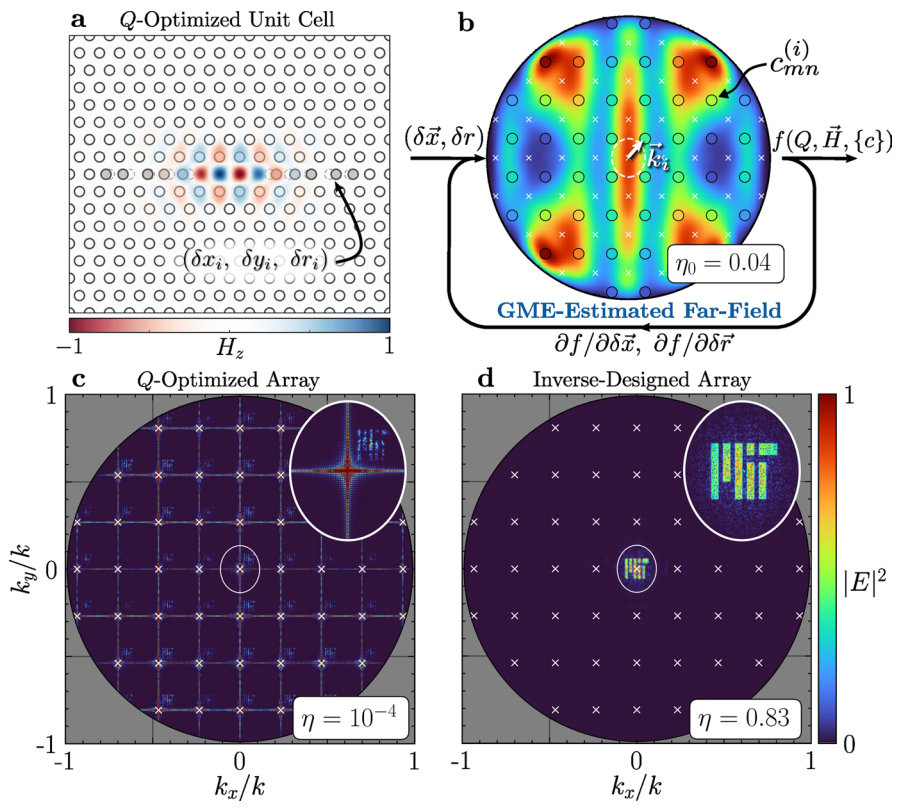
**Extended data** is available for this paper at https://doi.org/10.1038/s41566-022-01086-9.

**Supplementary information** The online version contains supplementary material available at https://doi.org/10.1038/s41566-022-01086-9.

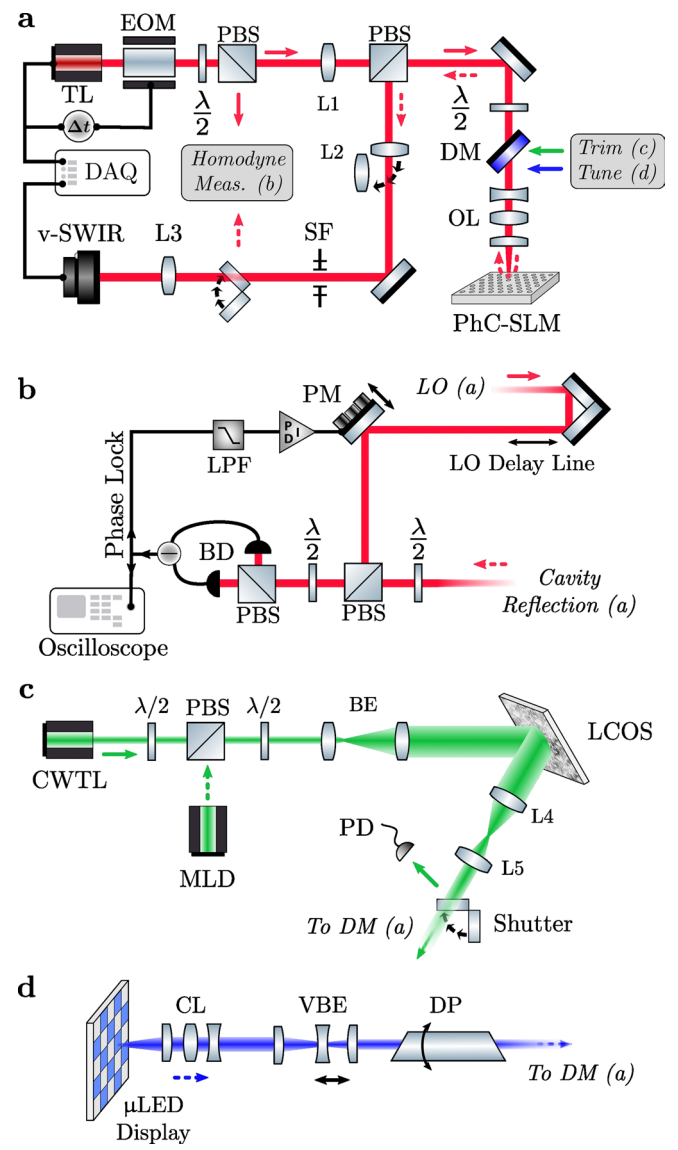
**Correspondence and requests for materials** should be addressed to Christopher L. Panuski or Dirk R. Englund.

**Peer review information** *Nature Photonics* thanks Subhojit Dutta, Volkan Gurses and the other, anonymous, reviewer(s) for their contribution to the peer review of this work.

**Reprints and permissions information** is available at www.nature.com/reprints.

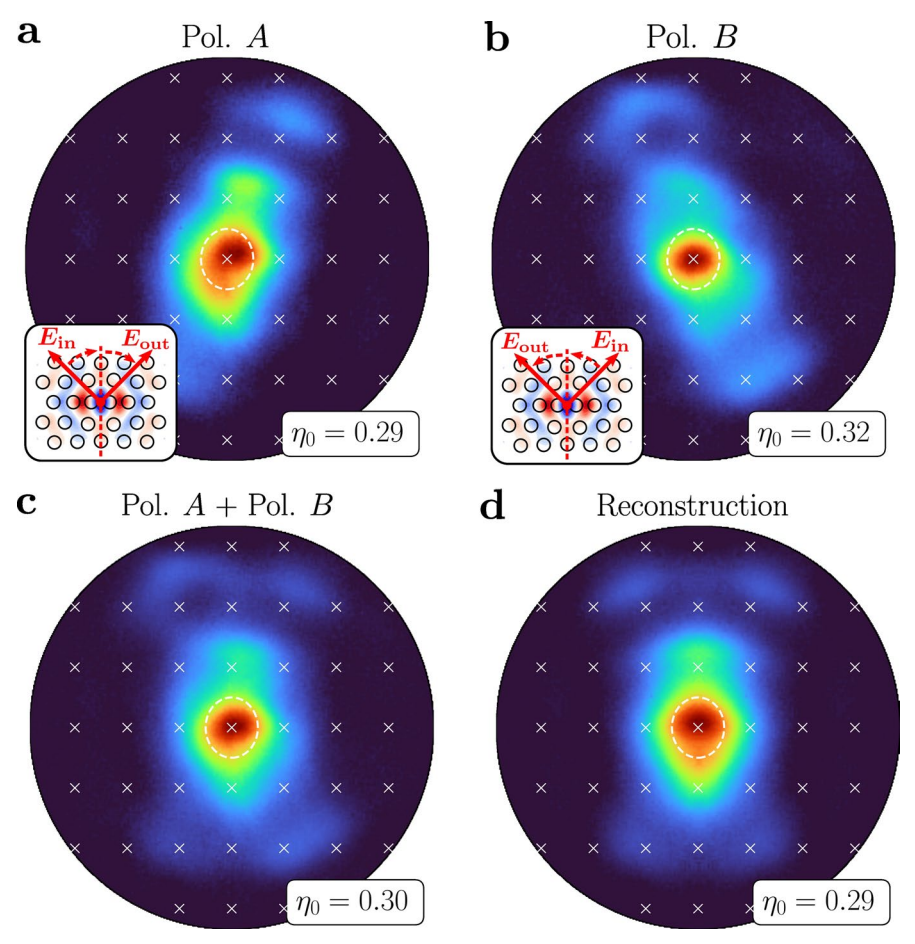


(Supplement Section D) have minimal overall diffraction efficiency  $\eta$ . Inverse design (b) solves these problems. Guided mode expansion (GME) approximates the mode's Q and far-field profile by sampling the losses  $\{c\}$  at the array's diffraction orders (white  $\times$  s) displaced by Bloch boundary conditions  $\vec{k}_i$  (that is at the coloured dots). An objective function f that maximizes Q, confines  $\vec{H}$ , and minimizes  $\{c\}$  at any non-zero diffraction order can then be efficiently optimized with respect to all hole parameters using reverse-mode automatic differentiation (b). The resulting devices with high-Q, efficient coupling, and directional emission enable high-performance ( $\eta$  - 1) resonant holography (d).



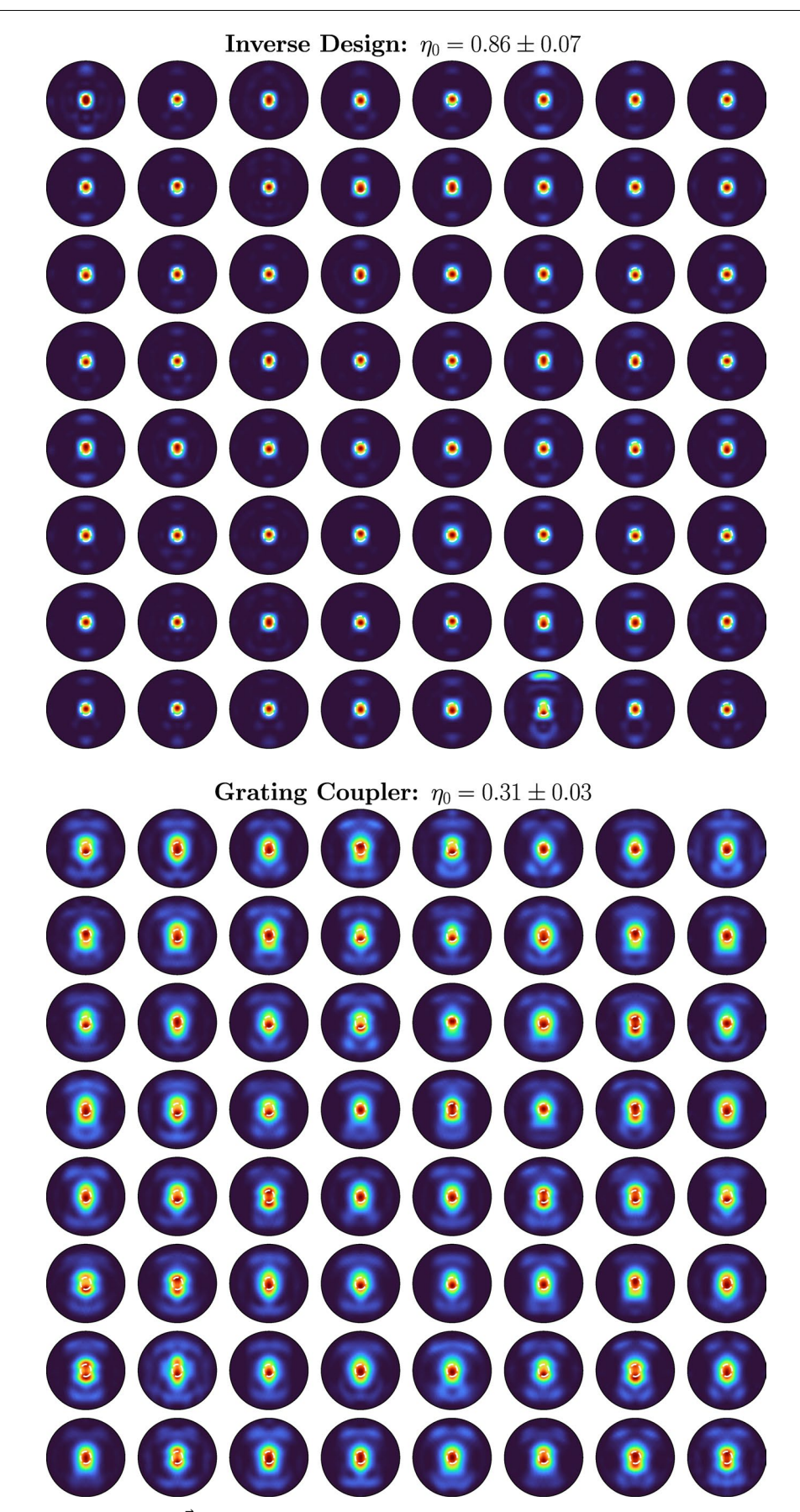
Extended Data Fig. 2 | Overview of experimental setups for measuring and controlling the photonic crystal SLM (PhC-SLM). A cross-polarized microscope (a) featuring balanced homodyne measurement (b) enables near-and far-field characterization of cavity arrays controlled by SLM-distributed coherent light (c) or high-speed incoherent µLED arrays (d). TL: tunable infrared laser (Santec TSL-710), EOM: electro-optic amplitude modulator;  $\lambda$ /2: half-wave plate, PBS: polarizing beamsplitter; L1: 250 mm back-focal-plane lens; DM: long-pass dichroic mirror; OL: objective lens (Nikon Plan Fluor  $40 \times /0.60$  NA or Nikon LU Plan  $100 \times /0.95$  NA), L2: 250 mm back-focal-plane lens; SF: spatial

filter; L3: 200 mm tube lens; v-SWIR: visible-short wave infrared camera (Xenics Cheetah 640); DAQ: data acquisition unit (NI USB-6343);  $\Delta t$ : trigger delay generator (SRS DG645); L0: local oscillator; PM: piezo mirror; BD: balanced detector (Thorlabs PDB480C-AC); Phase Lock: TEM LaseLock; LPF: low-pass filter; CWTL: continuous-wave trimming laser (Coherent Verdi V18); MLD: modulated laser diode (Hubner Cobolt or PicoLAS LDP); BE:  $5 \times v$  visible beam expander; LCOS: high-power liquid crystal SLM (Santec SLM-300); L4: 300 mm; L5: 250 mm; PD: photo-detector; CL: collection lens (Zeiss Fluar  $5 \times /0.25$  NA); VBE:  $0.5 \times -2 \times v$  variable beam expander; DP: dove prism.

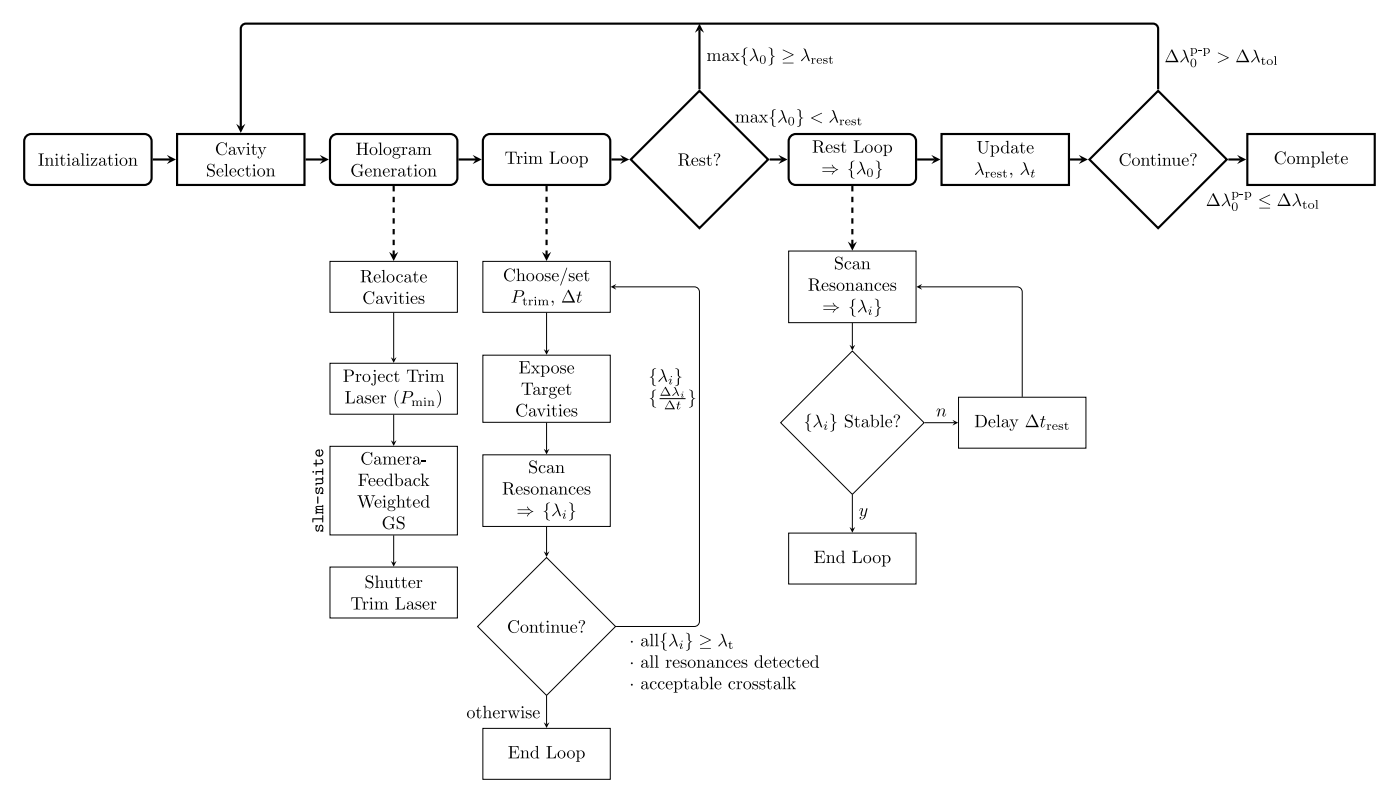


Extended Data Fig. 3 | Cross-polarized back-focal-plane (BFP) imaging techniques for a grating-coupled L3 cavity. Two orthogonally polarized far-field profiles are imaged by orienting the input polarization  $E_{\rm in}$  at a + 45° (a) or – 45° (b) angle from the dominant cavity polarization axis (dashed line in inset).

The complete cavity emission profile  $S(\vec{k})$  can be reconstructed by summing both images (c) or approximated from a single polarized image (d), yielding near-identical images with quantitative agreement between the extracted  $\eta_0$ .



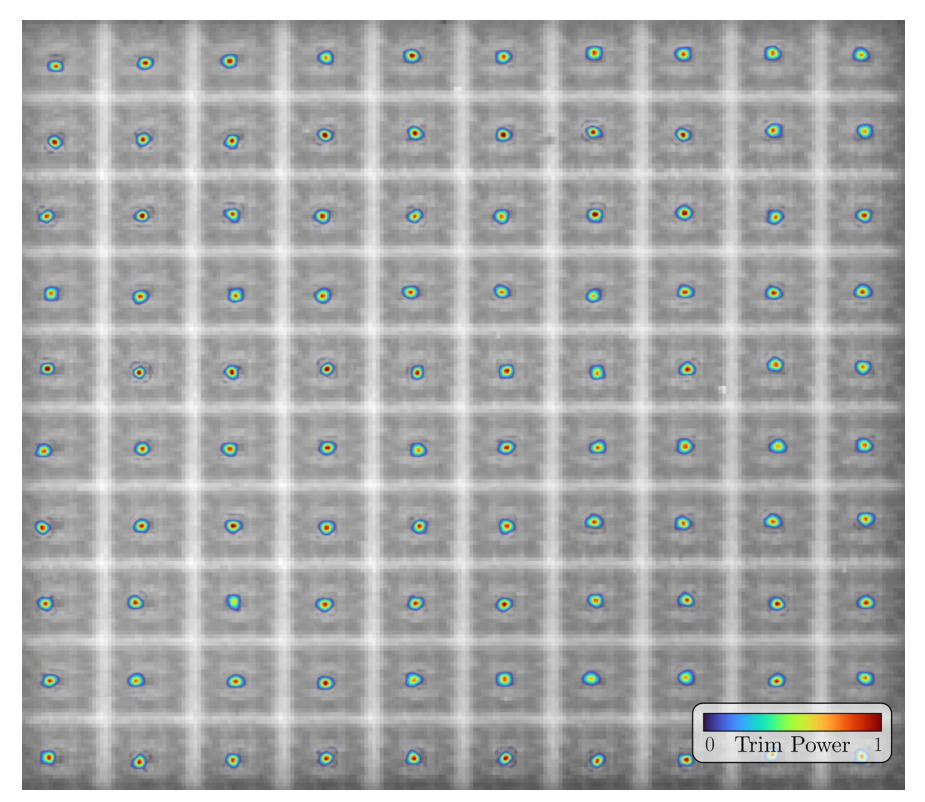
Extended Data Fig. 4 | Imaged far-field profiles  $S(\vec{k})$  (over a 0.9 numerical aperture) for each device in an 8  $\times$  8 array of inverse designed (top) and grating-coupled (bottom) L3 PhC cavities. The extracted zero-order efficiencies  $\eta_0$  and standard deviations are also provided.



#### $Extended\ Data\ Fig.\ 5 \ |\ Flow chart\ of\ the\ holographic\ trimming\ algorithm.$

Trimming holograms are formed with weighted Gerchberg-Saxton (GS) algorithms and projected onto desired cavities for duration  $\Delta t$  with power  $P_{\text{trim}}$ . Alternating trimming and resonance readout periods continue until the instantaneous wavelength  $\lambda_i$  of any targeted cavity blueshifts past the target wavelength  $\lambda_r$ . Thereafter, a new set of target cavities is selected and trimmed. This selection and trimming sub-loop continues until all resonant wavelengths  $\{\lambda_0\}$  are below the 'rest' wavelength  $\lambda_{\text{rest}}$ , at which point trimming is halted and the

resonances are continuously monitored at readout interval  $\Delta t_{\rm rest}$ . When the resonances are sufficiently stable (redshifting from moisture adsorption to the silicon membrane is arrested), the total 'rehydration' redshift  $\Delta \lambda_0$  of each cavity is updated to better estimate the true resonant wavelength  $\lambda_0 \approx \lambda_i + \Delta \lambda_0$  from the instantaneous wavelengths  $\{\lambda_i\}$  during trimming. The entire process terminates when the peak-to-peak static resonant wavelength uniformity  $\Delta \lambda_0^{p-p}$  drops below the desired tolerance  $\Delta \lambda_{\rm tol}$ .



Extended Data Fig. 6 | Overlaid images of  $10\times10$  cavity (grey) and trimming spot (colour) arrays demonstrating the  $\ll$   $\mu m$  placement accuracy and percent-order power uniformity of weighted Gerchberg-Saxton phase

 $\label{lem:continuous} \textbf{retrieval with experimental camera feedback.} \ In \ general, our holography software (Supplement Section F) \ creates high-uniformity optical foci to arbitrary image plane locations specified by the user.$ 

Extended Data Table 1 | Performance comparison of our PhC-SLM (bold) to selected active 2D spatial light modulators from Fig. 1b. Estimated fill factors  $\zeta$  are marked by a \*. Wavelength-steered devices <sup>100</sup> are excluded to focus on active, individually-addressable arrays

Class [Year]	Device	$N_x \times N_y$	$\Omega_{\rm s} = \frac{\lambda}{\Lambda_{\rm r}} \times \frac{\lambda}{\Lambda_{\rm r}}$	ζ[%]	ω <sub>s</sub> /2π [Hz]
EO [2022]	PhC-SLM	8×8	10.6°×14.5°	64	1.4 × 10 <sup>8</sup>
EO [2021]	$\chi^{(2)}$ polymer-coated grating $^{73}$	2×2	0.2°×0.2°	_	5.0×10 <sup>7</sup>
EO [2019]	$\chi^{\!\scriptscriptstyle{(3)}}$ thin-film plasmonic resonator $^{\scriptscriptstyle{71}}$	4×4	0.8°×1.1°	20*	1.0×10 <sup>9</sup>
EO [2017]	Bilayer guided resonators <sup>79</sup>	6×6	0.3°×0.3°	40*	2×10 <sup>8</sup>
EO [2015]	Waveguided p-i-n modulators <sup>101</sup>	4×4	1.8°×1.8°	10*	2×10 <sup>8</sup>
EO [2011]	$\chi^{(2)}$ polymer-coated grating $^{63}$	4×4	0.1°×0.1°	18*	8.0×10 <sup>5</sup>
EO [2005]	MQW micropillar modulators 102	128×128	1.3°×1.3°	50	1.3×10 <sup>7</sup>
Thermal [2018]	Asymmetric Fabry-Perot cavity 35	6×6	3.4°×3.4°	59	1.4×10 <sup>4</sup>
Thermal [2013]	Waveguided phased array 12,103	8×8	9.9°×9.9°	10*	1.1×10⁵
MEMS [2019]	Grating phase shifters <sup>65</sup>	160×160	4.4°×4.1°	85*	5.5×10 <sup>4</sup>
MEMS [2019]	Piston mirrors <sup>104</sup>	960×540	3.4°×3.4°	_	2.0×10 <sup>4</sup>
MEMS [2014]	High-contrast gratings <sup>64</sup>	8×8	2.7°×2.7°	36*	5.0×10 <sup>5</sup>
MEMS [2001]	Piston mirrors <sup>105</sup>	256×256	0.9°×0.9°	86	5.0×10 <sup>5</sup>
LC [2020]	Plasmonic metasurface 106	3×2	0.3°×0.3°	-	2.5×10¹
LC [2019]	'MacroSLM' 107	1536×1536	3.0°×3.0°	95	6.0×10 <sup>2</sup>
LC [1994]	Binary ferroelectric LC <sup>108</sup>	256×256	2.2°×2.2°	79	8.3×10 <sup>3</sup>

Extended Data Table 2 | Comparison of previous microcavity array trimming techniques to our parallel laser assisted thermal oxidation (bold). Estimated values are marked with a \*.  $\Delta\lambda_{p-p}$  = peak-to-peak wavelength error; Q = mean quality factor

Technique [Year]	Cavity Type	N	$\Delta \lambda_0^{p-p}$ [pm]	Q	In situ?	Parallel?	
'Holographic' oxidation [2022]	Si PhC	64	13	2×10 <sup>5</sup>	Y	Y	
Germanium implantation [2021]	Si ring <sup>109</sup>	58	32	4×10³	Υ	N	
Laser-annealed cladding [2020]	Si ring 110	2	20*	2×10 <sup>4</sup>	Υ	N	
Boron implantation [2019]	Si ring <sup>111</sup>	4	15	5×10³	Υ	N	
Electron-beam irradiation [2018]	Si PhC 112	4	400	3×10⁵	N	N	
Photo-electro-chemical etching [2017]	GaAs disk <sup>113</sup>	5	200*	2×10 <sup>4</sup>	Υ	N	
Annealed cladding [2016]	Si ring 114	5	90*	3×10³	Υ	N	
Ultraviolet irradiation [2014]	a-Si ring <sup>115</sup>	4	45	8×10³	Υ	N	
Post-fabrication etching [2013]	GaAs PhC 116	18	100*	3×10 <sup>4</sup>	N	Υ	
Photochromatic thin-film [2011]	GaAs PhC 117	3	340	8×10³	Υ	N	
Anodic oxidation [2006]	GaAs PhC 118	2	100*	5×10³	N	N	